

Supporting Information

Ultrafast and Efficient Energy Transfer in a One- and Two-Photon Sensitized Rhodamine-BODIPY Dyad: A Perspective for Broadly Absorbing Photocages

Marvin Asido^{†,a}, Carsten Hamerla^{†,a}, Rebekka Weber^{†,b}, Maximiliane Horz^{†,a},
Madhava Shyam Niraghatam^a, Alexander Heckel^{*,b}, Irene Burghardt^{*,a} and
Josef Wachtveitl^{*,a}

^aInstitute of Physical and Theoretical Chemistry and ^bInstitute of Organic Chemistry and
Chemical Biology, Goethe University Frankfurt, Max-von-Laue Straße 7, 60438 Frankfurt
am Main, Germany

Table of content

- General procedures
- Synthesis
- Experimental details
- Supplementary spectroscopic data
- Theoretical investigation
- NMR- and mass spectra

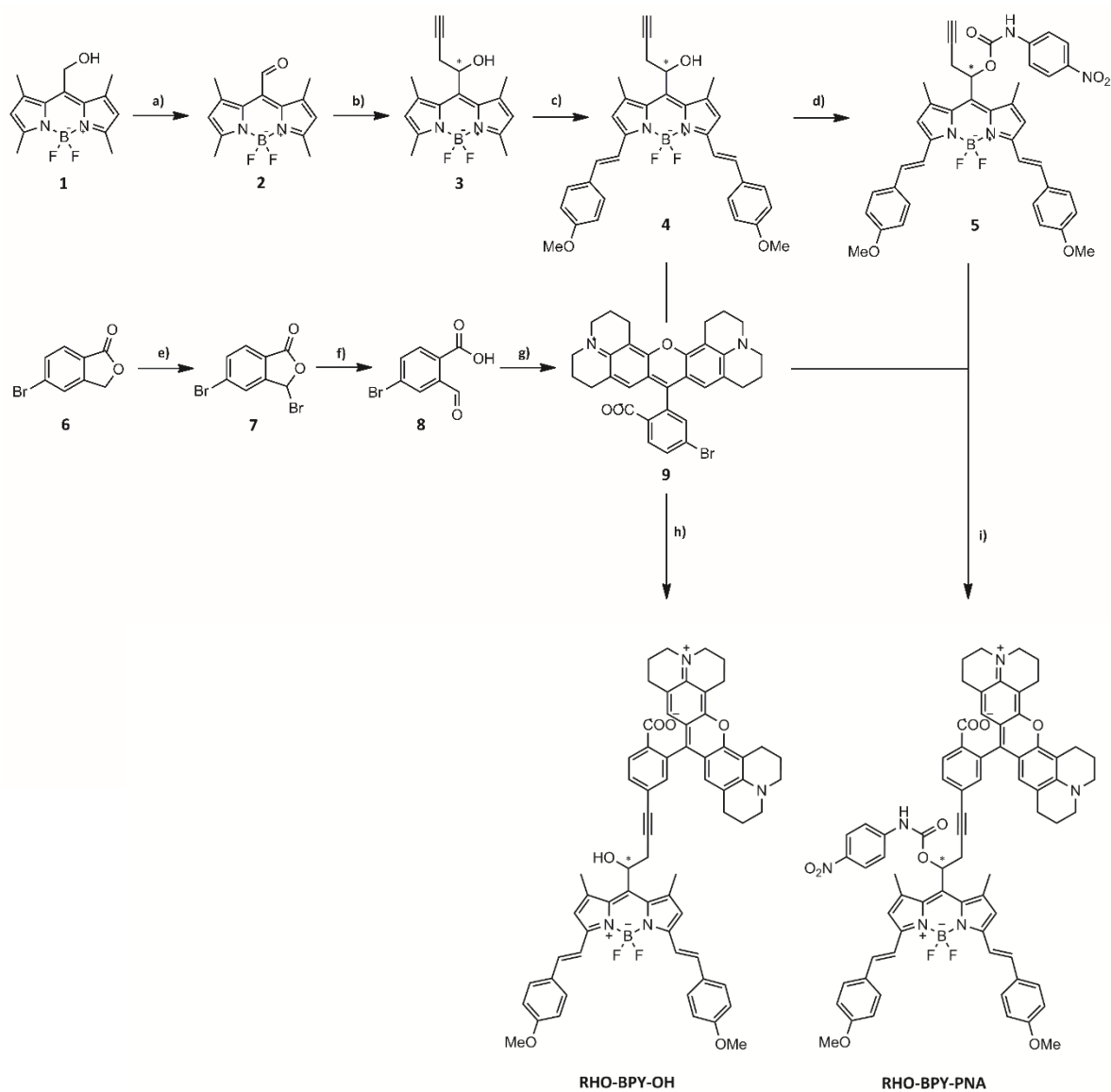
General procedures

Chemicals were purchased from commercial suppliers (*Sigma Aldrich, Acros Organics, TCI, Alfa Aesar, VWR*) and used without further purification. If not otherwise specified, reactions were performed under argon atmosphere, in the dark and in dry solvents. Microwave reactions were conducted in a *Biotage Initiator EXP EU* microwave system using sealed microwave vials. Control of the reaction progress was monitored by TLC using silica 60 aluminium sheets with fluorescence indicator UV₂₅₄ from *Macherey-Nagel*. Detection was carried out with UV-light at wavelengths 254 nm and 366 nm. Crude products were purified by column chromatography either manually with silica gel 60 from *Macherey-Nagel* or automated by flash chromatography with a *PuriFlash XS 420* device and appropriate silica gel columns (30 μm or 50 μm) from *Interchim*.

NMR spectroscopic analysis was carried out with a 500 MHz device from *Bruker*. Samples were prepared using deuterated solvents by *euriso-top*. Spectra were analysed using *TopSpinTM* software by *Bruker*. The chemical shift of ^1H and $^{13}\text{C}\{^1\text{H}\}$ spectra was calibrated with solvent signal of CDCl_3 (δ (ppm) = 7.26 for ^1H and 77.16 for $^{13}\text{C}\{^1\text{H}\}$) and DMSO-d_6 (δ (ppm) = 2.50 for ^1H and 39.52 for $^{13}\text{C}\{^1\text{H}\}$). SiMe_4 served as external standard for ^1H and $^{13}\text{C}\{^1\text{H}\}$ spectra, while $\text{BF}_3\cdot\text{OEt}_2$ was used for $^{11}\text{B}\{^1\text{H}\}$ spectra and CFCl_3 was used for ^{19}F spectra. High resolution mass spectra (HRMS) were obtained from a MALDI *LTQ Orbitrap XL* instrument from *ThermoScientific*.

Synthesis

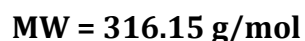
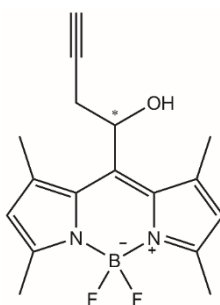
Compound 1 & 2¹ and 6 - 9² were synthesized according to literature.



Scheme S1. Synthetic route of the formation of RHO-BPY-OH and RHO-BPY-PNA.

- a)** Dess-Martin-periodinane, DCM, 1.5 h, 0 °C → rt, 82%; **b)** Zn, propargyl bromide, DMF, 1 h, 0 °C, 89%; **c)** *p*-anisaldehyde, piperidine, 2 h, 60 °C, 50%; **d)** 4-nitrophenyl isocyanate, TEA, toluene, 7 h, 50 °C, 78%; **e)** NBS, AIBN, CHCl₃, 9 h, 70 °C, 56%; **f)** H₂O, 4 h, 90 °C, 80%; **g)** 8-Hydroxyjulolidine, *p*-TsOH, chloranil, propionic acid, 16 h, 80 °C, 69%; **h)** Pd(PPh₃)₄, CuI, TEA, n-propanol, methanol, 2.5 h, 80 °C, 63%; **i)** Pd(PPh₃)₄, CuI, TEA, n-propanol, methanol, 3 h, 70 °C, 27%.

8-(1-Hydroxybut-3-yn-1-yl)-1,3,5,7-tetramethyl-pyrromethene-fluoroborate (3)



A suspension of preactivated zinc chips (414 mg, 6.3 mmol, 5.0 eq.) in 5 ml DMF was cooled to 0 °C. After addition of propargyl bromide (0.14 ml, 1.9 mmol, 1.5 eq.) the mixture stirred for 1 h in the cold. **3** (350 mg, 1.3 mmol, 1.0 eq.) was added in 10 ml DMF and the reaction continued stirring at 0 °C until completion followed by TLC. The reaction was quenched with saturated NH₄Cl solution and extracted three times with diethyl ether. The organic layers were washed with H₂O and brine and dried over MgSO₄. The solvent was removed in vacuo yielding 89% of **3** (357 mg, 1.1 mmol) as orange-green solid.

¹H NMR (500 MHz, CDCl₃): δ = 6.10 (s, 2H), 5.70 (dd, *J*₁ = 10.1 Hz, *J*₂ = 3.8 Hz, 1H), 3.03 – 2.95 (m, 1H), 2.69 – 2.62 (m, 1H), 2.52 (s, 6H), 2.50 (s, 6H), 2.18 (t, *J* = 2.7 Hz, 1H) ppm.

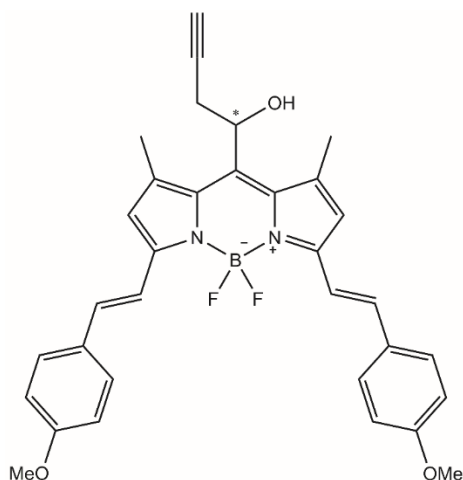
¹³C{¹H} NMR (126 MHz, CDCl₃): δ = 155.9, 143.5, 130.9, 123.3, 79.8, 71.9, 66.9, 29.7, 26.8, 14.6 ppm.

¹¹B{¹H} NMR (160 MHz, CDCl₃): δ = 0.48 (t, *J* = 32.4 Hz) ppm.

¹⁹F NMR (471 MHz, CDCl₃): δ = -146.2 (q, *J* = 33.1 Hz) ppm.

MALDI-HRMS: *m/z* calcd for C₁₇H₁₉BF₂N₂O [M·]⁺: 316.15530, found 316.15543 (Δ*m* = 0.00013).

8-(1-Hydroxybut-3-yn-1-yl)-1,7-dimethyl-3,5-(bis(4-methoxystyryl))-pyrromethene-fluoroborate (4)



MW = 552.42 g/mol

3 (210 mg, 0.7 mmol, 1.0 eq.) was dissolved in *p*-anisaldehyde (4.0 ml, 33 mmol, 50 eq.). After addition of a few drops piperidine the reaction mixture was stirred for 2 h at 60 °C. The crude mixture was loaded on a silica column and purified using cyclohexane/ ethyl acetate (CH/EE (2/1): R_f = 0.36) as eluent. The product was obtained with 50% yield (184 mg, 0.3 mmol) as dark blue solid.

¹H NMR (500 MHz, CDCl₃): δ = 7.62 – 7.54 (m, 6H), 7.21 (d, *J* = 16.1 Hz, 2H), 6.94 – 6.90 (m, 4H), 6.71 (s, 2H), 5.73 (dd, *J*₁ = 10.0 Hz, *J*₂ = 4.3 Hz, 1H), 3.85 (s, 6H), 3.05 – 2.98 (m, 1H), 2.72 – 2.65 (m, 1H), 2.55 (s, 6H), 2.18 (t, *J* = 2.5 Hz, 1H) ppm.

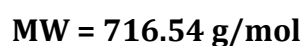
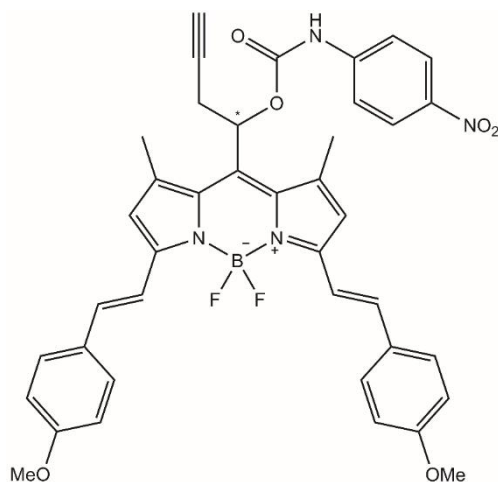
¹³C{¹H} NMR (126 MHz, CDCl₃): δ = 160.7, 153.0, 139.5, 136.4, 133.0, 129.7, 129.3, 119.7, 117.3, 114.4, 80.2, 71.9, 67.1, 55.5, 29.9, 27.1 ppm.

¹¹B{¹H} NMR (160 MHz, CDCl₃): δ = 0.94 (t, *J* = 34.2 Hz) ppm.

¹⁹F NMR (471 MHz, CDCl₃): δ = -138.0 (q, *J* = 28.7 Hz) ppm.

MALDI-HRMS: *m/z* calcd for C₃₃H₃₁BF₂N₂O₃ [M]⁺: 552.23903, found 552.23817 (Δ*m* = 0.00086).

8-(1-(OCO-PNA)-but-3-yn-1-yl)-1,7-dimethyl-3,5-(bis(4-methoxystyryl))-pyrromethene-fluoroborate (5)



To a solution of **4** (75 mg, 136 μ mol, 1.0 eq.) in 4 mL toluene in a microwave vial, 4-nitrophenyl isocyanate (89 mg, 543 μ mol, 4.0 eq.) and triethylamine (7.5 μ l, 54.3 μ mol, 0.4 eq.) were added. The reaction was performed in the microwave for 7 h at 50 °C. The crude mixture was diluted with ethyl acetate and then washed twice with NH₄Cl solution and once with brine. The organic layers were dried over MgSO₄ and concentrated in vacuo. The residue was purified by column chromatography using cyclohexane/ ethyl acetate (CH/EE (2/1): R_f = 0.27) as eluent to obtain **5** in 78% yield (76 mg, 106 μ mol) as blue solid.

¹H NMR (500 MHz, CDCl₃): δ = 8.19 (d, *J* = 9.2 Hz, 2H), 7.62 – 7.53 (m, 8H), 7.20 (d, *J* = 16.3 Hz, 1H), 6.98 – 6.88 (m, 6H), 6.77 (d, *J* = 11.4 Hz, 2H), 3.85 (s, 6H), 3.20 – 3.13 (m, 1H), 2.93 – 2.87 (m, 1H), 2.74 (s, 3H), 2.58 (s, 3H), 2.11 (t, *J* = 2.6 Hz, 1H) ppm.

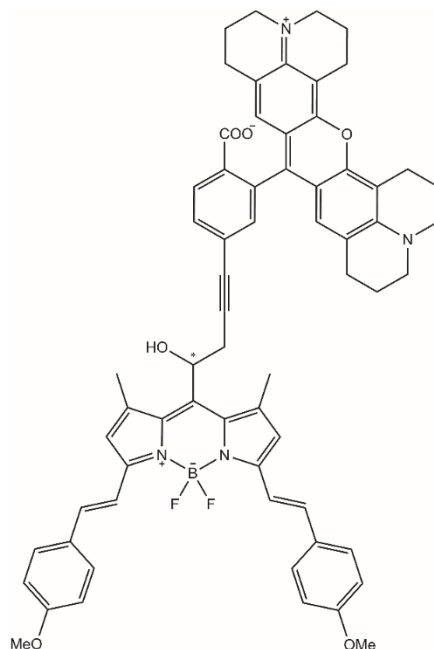
¹³C{¹H} NMR (126 MHz, CDCl₃): δ = 152.5, 151.8, 143.6, 143.3, 137.8, 136.2, 134.2, 129.5, 129.3, 126.5, 125.3, 118.4, 114.5, 113.5, 78.2, 72.2, 68.8, 55.5, 29.8, 25.5, 18.8, 18.3 ppm.

¹¹B{¹H} NMR (160 MHz, CDCl₃): δ = 0.94 (t, *J* = 33.8 Hz) ppm.

¹⁹F NMR (471 MHz, CDCl₃): δ = -137.9 (q, *J* = 30.8 Hz) ppm.

MALDI-HRMS: m/z calcd for $C_{40}H_{35}BF_2N_4O_6$ $[M]^+$: 716.26122, found 716.26093 ($\Delta m = 0.00029$).

Rho-BPY-OH



MW = 1040.99 g/mol

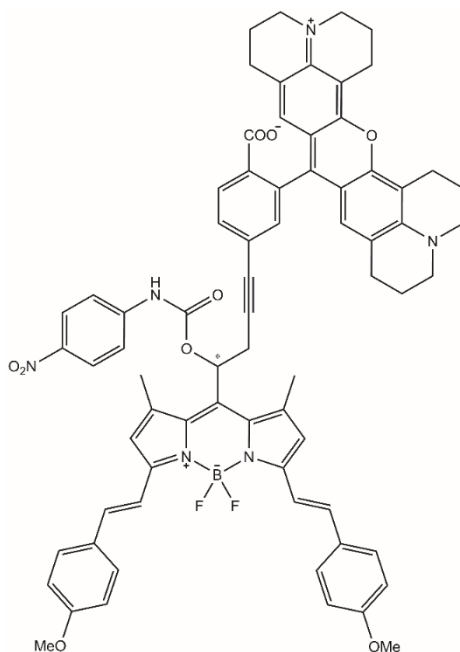
Compound **9** (35 mg, 61 μ mol, 1.0 eq.) and **4** (41 mg, 74 μ mol, 1.2 eq.) were solved in a mixture of 2 ml n-propanol, 2 ml methanol and 0.1 ml triethylamine in a microwave vial. After addition of $Pd(PPh_3)_4$ (5.7 mg, 4.9 μ mol, 0.08 eq.) and CuI (1.9 mg, 9.8 μ mol, 0.16 eq.) the reaction was heated in the microwave for 2.5 h at 80 °C. The crude reaction mixture was purified by column chromatography using DCM/ methanol (DCM/MeOH (9/1): $R_f = 0.55$) as eluent to obtain **RHO-BPY-OH** in 63% yield (40 mg, 39 μ mol) as purple solid.

1H NMR (500 MHz, DMSO- d_6): $\delta = 7.98 - 7.94$ (m, 2H), 7.59 - 7.52 (m, 8H), 7.50 - 7.44 (m, 2H), 7.08 - 7.03 (m, 5H), 6.29 (s, 2H), 3.82 (s, 6H), 3.19 - 3.12 (m, 1H), 3.04 - 3.01 (m, 4H), 2.83 - 2.79 (m, 1H), 2.66 - 2.61 (m, 6H), 1.99 - 1.93 (m, 4H), 1.82 - 1.77 (m, 4H) ppm.

$^{13}\text{C}\{^1\text{H}\}$ NMR (126 MHz, CDCl_3): δ = 160.6, 152.2, 140.2, 132.3, 132.2, 129.2, 128.7, 117.2, 114.4, 113.3, 104.9, 55.6, 45.9, 37.2, 32.9, 32.1, 29.8, 27.6, 27.2, 22.8, 19.9 ppm.

MALDI-HRMS: m/z calcd for $\text{C}_{65}\text{H}_{59}\text{BF}_2\text{N}_4\text{O}_6$ $[\text{M}+\text{H}]^+$: 1041.45685, found 1041.45801 (Δm = 0.00116).

Rho-BPY-PNA



$\text{C}_{72}\text{H}_{63}\text{BF}_2\text{N}_6\text{O}_9$

MW = 1205.11 g/mol

Compound **9** (36 mg, 63 μmol , 1.0 eq.) and **5** (68 mg, 95 μmol , 1.5 eq.) were solved in a mixture of 4 ml n-propanol, 4 ml methanol and 0.2 ml triethylamine in a microwave vial. After addition of $\text{Pd}(\text{PPh}_3)_4$ (7.3 mg, 6.3 μmol , 0.1 eq.) and CuI (0.9 mg, 5.1 μmol , 0.08 eq.) the reaction was heated in the microwave for 3 h at 70 $^\circ\text{C}$. The crude reaction mixture was purified by column chromatography using $\text{DCM}/\text{methanol}/\text{triethylamine}$ (100/ 3.5/ 1.5) as eluent to obtain **RHO-BPY-PNA** in 27% yield (21 mg, 17 μmol) as purple solid.

^1H NMR (500 MHz, CDCl_3): δ = 8.05 – 8.02 (m, 2H), 7.73 – 7.70 (m, 2H), 7.59 – 7.56 (m, 2H), 7.36 – 7.29 (m, 8H), 6.93 – 6.89 (m, 5H), 6.65 – 6.60 (m, 2H), 6.27 (s, 1H), 6.23 (s, 1H),

4.84 – 4.80 (m, 1H), 3.77 (s, 6H), 3.49 – 3.45 (m, 8H), 3.12 – 3.05 (m, 4H), 2.90 – 2.88 (m, 1H), 2.74 – 2.72 (m, 1H), 2.02 – 1.99 (m, 4H), 1.83 – 1.80 (m, 4H) ppm.

MALDI-HRMS: m/z calcd for $C_{72}H_{63}BF_2N_6O_9$ $[M+H]^+$: 1205.47904, found 1205.47905 ($\Delta m = 0.00001$).

Experimental details

Steady-state absorption experiments

The steady-state spectra of the samples were recorded with a spectrometer (Specord 600, Analytic Jena, Germany) before and after each experiment to check for significant sample degradation. For the illumination experiments we used a customized sample holder, which was connected to a thermostat (SC 150, Thermo Fisher Scientific, USA). Illumination was done with an LED (M565L3, Thorlabs, USA) at 565 nm and 660 nm. The energies were set to 40 mW/ cm² at the sample position. The samples were placed in a 10x4 mm cuvette with a resulting optical pathlength of 10 mm and an orthogonal illumination pathway of 4 mm. The samples were thermally equilibrated at 20 °C before absorption spectra (with 30 seconds pre-irradiation time) were taken. After thermal equilibration and a mixing period of 30 minutes with a magnetic stirrer, spectra were taken in 30 s intervals over a time window of 6000 s resulting in 200 spectra. After baseline correction, the differences were then calculated by subtracting the first (dark) spectrum from the remaining spectra.

Steady-State fluorescence experiments

The fluorescence quantum yield ϕ_F was determined by using an integrative sphere (ILF-835, Jasco, Germany), attached to a fluorescence spectrometer (FP-8500, Jasco, Germany). Spectra were taken in the range from 250 nm to 900 nm with a spectral resolution of 2 nm. The PMT voltage was adjusted to 440 V to achieve the maximum fluorescence signal without saturation of the detector. For reference and sample measurements, 4x10 mm Quartz cuvettes were employed. To avoid reabsorption effects, the OD of the respective rhodamine samples was adjusted to ~ 0.1 (10 mm optical path length). The solvent (MeOH) was used as reference. The reference signal (mainly the stray light of the solvent and the cuvette) was subtracted from the sample signal. The ϕ_F was determined by calculating the ratio between the residual fluorescence and the excitation integrals.

Processing and quantum yield calculation were performed with the Jasco software package (Spectra Manager Suite).

Two-photon excitation fluorescence experiments

For the two-photon excitation fluorescence (TPEF) measurements we used a tunable Ti:Sa laser (Tsunami, Spectra-Physics, USA) with a pulse duration of 150 fs and a 80 MHz repetition rate. The excitation was adjusted to an average energy of 500 mW. The pulses were then tightly focused onto the sample compartment. The TPEF-signal was coupled into a spectrograph (SpectraPro 300i, Acton Research Corp., USA), which is equipped with a CCD-camera (EEV 400_1340F, Roper Scientific, USA). To obtain the two-photon absorption spectrum we determined the two-photon absorption action cross sections in the range of 770-870 nm. We used Rhodamin 6G as reference, using the following equation³⁻⁶

$$\phi_F(X) \sigma_2(X) = \sigma_2(R) \cdot \phi_F(R) \frac{I_F(X) \cdot c(R) \cdot \eta(R)}{I_F(R) \cdot c(X) \cdot \eta(X)} \quad (1)$$

where σ_2 = two-photon absorption cross section, ϕ_F =fluorescence quantum yield, X =sample, R = reference, I_F = fluorescence intensity, c =concentration, η =refractive index of the solvent. We furthermore assumed the one-photon fluorescence quantum yield to be equal to the two-photon fluorescence quantum yield.^{3,6} The values for the reference compound were taken from Makarov et al.⁴ The concentrations for the rhodamine samples, as well as the Rhodamine 6G reference were adjusted to 100 μ M.

Time-correlated single photon counting experiments

The fluorescence decay of the rhodamine antennas was determined by the time-correlated single photon counting (TCSPC) technique. Our home-built TCSPC setup is composed of a single-photon detection photomultiplier tube (PMA-C 182 M, PicoQuant, Germany) and a PCIe card (TimeHarp 260 PICO Single, PicoQuant) for sub-ns data processing. Pulsed orthogonal excitation of the samples was achieved by a pulsed LED (LDH-PC-510B, PicoQuant) with a FWHM < 110 ps. Deconvolution with the IRF and multi-

exponential fitting of the temporal traces was performed with FluoFit Pro 4.6 (PicoQuant) based on the following equation⁷

$$I(t) = \int_{-\infty}^t IRF(t') \sum_{i=1}^n A_i e^{-\frac{t-t_i}{\tau_i}} dt' \quad (2)$$

The samples were measured in 4 × 10 mm quartz glass cuvettes with the same conditions as given in the steady state fluorescence measurements.

Femtosecond UV/vis-pump-probe experiments

The time-resolved transient absorption measurements were performed using a home-built pump-probe setup. A Ti:Sa chirped pulse regenerative amplifier (MXR-CPA-iSeries, Clark-MXR Inc., USA) with a central output wavelength of 775 nm, a 1 kHz repetition rate, and a pulse width of 150 fs was used as the fs-laser source. The fundamental was split for pump and probe pulse generation. Pump pulses at a central wavelength of 560 nm and 660 nm were generated in a two-stage NOPA process and temporally compressed to a FWHM of ~75-80 fs. In both cases, the excitation energy was set to 90 nJ/pulse at the sample position. The supercontinuum for the probe pulses was generated by focusing the fundamental in a constantly moving CaF₂ window of 5 mm thickness, leading to stable white light in the range of 375-700 nm. The white light was then split and guided through the sample and the reference arm of the detection setup. Each arm makes use of a spectrograph (Multimode, AMKO, Germany), which is equipped with two gratings (300 nm/ 500 nm blaze, 600/1200 grooves per mm), a photodiode array (S8865-64, Hamamatsu Photonics, Japan) and a corresponding driver circuit (C9118, Hamamatsu Photonics, Japan). The signals were digitized by a 16 bits data acquisition card (NI-PCI-6110, National Instruments, USA). The pump and probe pulses were set to the magic angle configuration at 54.7° to account for anisotropic effects. The sample-compartment was constantly moved to minimize sample degradation.

Kinetic analysis of the ultrafast spectroscopic data

The analysis of our experimental data was done by OPTIMUS.⁸ For the ultrafast TA measurements, we used the lifetime distribution analysis (LDA). Within this method a quasi-continuous sum of exponentials is used to allow a model independent analysis of the data. The pre-exponential factors of a set amount of exponential functions, in this case 100, with fixed and equally distributed lifetimes were determined and plotted in a contour representation (lifetime density map, LDM). For a further read on the methodology see (www.optimusfit.org).

Supplementary spectroscopic data

Structures of tested rhodamine compounds

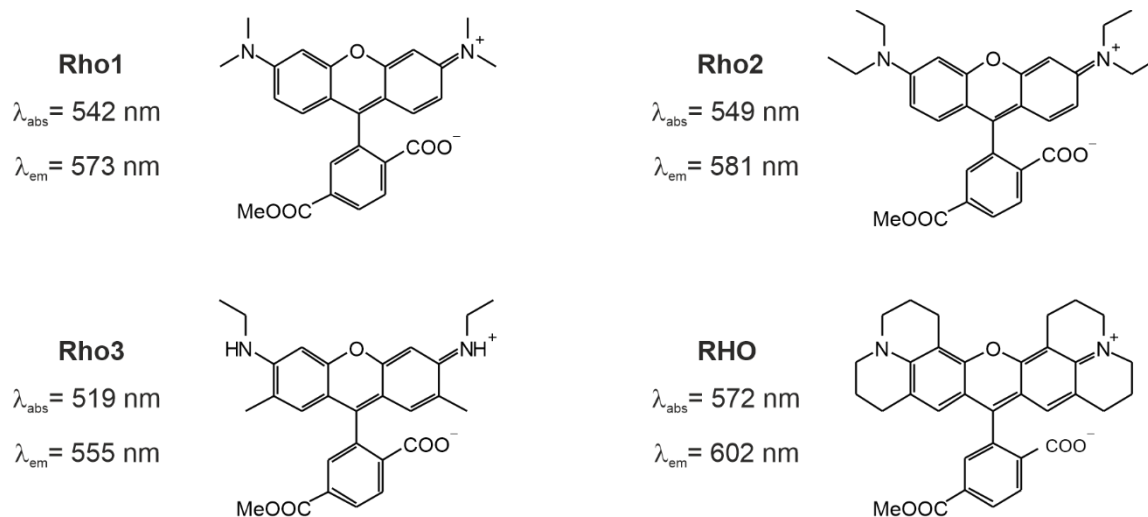


Figure S1. Chemical structures of Rho1-3 and RHO with their respective absorption and fluorescence maxima.

Steady state absorption / fluorescence spectra of rhodamine compounds

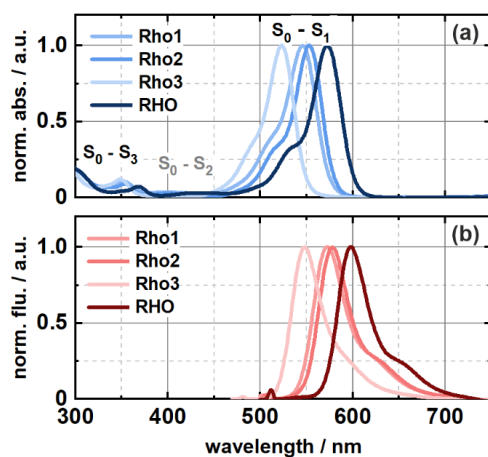


Figure S2. (a) Normalized absorption spectra of Rho1-3 and RHO and (b) their corresponding fluorescence spectra.

Table S1. Fluorescence quantum yields and molar extinction coefficients of Rho1-3 and RHO.

	Rho1	Rho2	Rho3	RHO
ϕ_F	0.41	0.47	0.9	0.84
$\epsilon / M^{-1} cm^{-1}$	86540	67190	69860	116780

Determination of 2P action cross sections

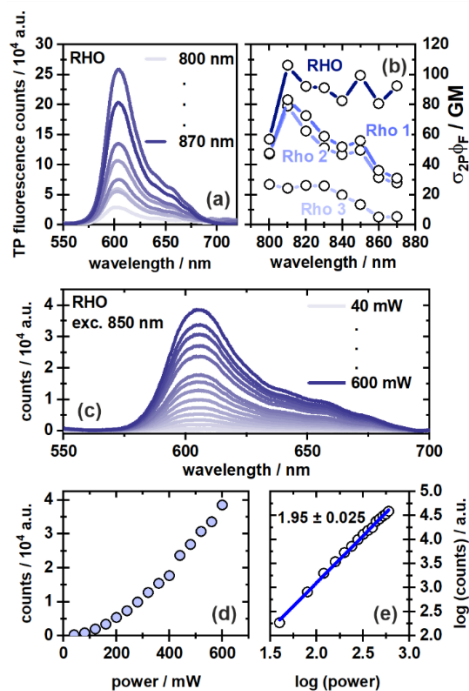


Figure S3. TPEF experiments of RHO. (a) Fluorescence response as a function of excitation wavelength. (b) Comparison of calculated 2P action cross-sections. (c) Fluorescence response as a function of excitation power at a fixed wavelength of 850 nm. Peak intensity of the fluorescence signal as a function of power on a (d) linear scale and (e) logarithmic scale. RHO shows an almost perfect quadratic dependency on excitation power.

Fluorescence lifetime of rhodamine compounds

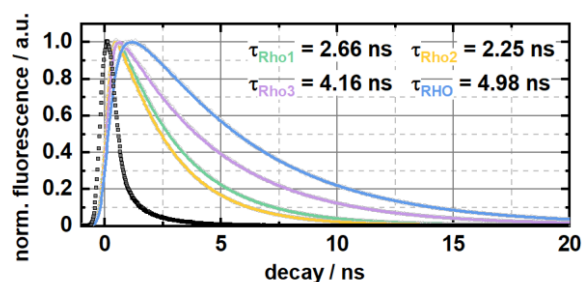


Figure S4. Time-traces of the TCSPC measurements. The IRF (grey dots) sets the lower limit of the temporal resolution. With a lifetime of almost 5 ns, RHO shows the slowest decay of the excited state.

Ultrafast TA measurements

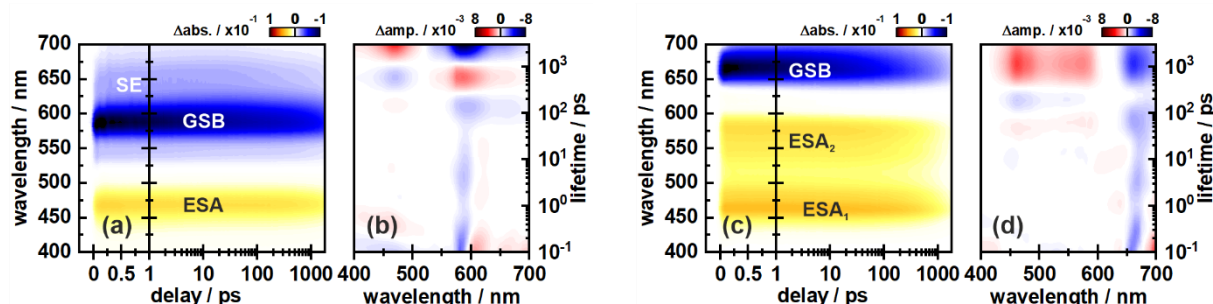


Figure S5. Ultrafast TA measurement of RHO (a) with an excitation at 565 nm and BPY (c) with an excitation at 660 nm and their corresponding LDMs (b) and (d). The LDM of RHO (b) shows a very slow excited state decay, which is in line with the lifetime found in the TCSPC measurement.

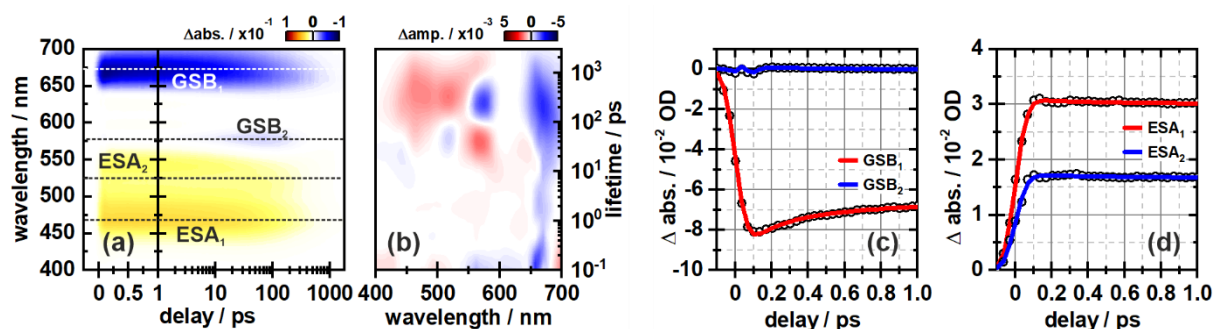


Figure S6. Ultrafast TA measurement of RHO-BPY-OH with an excitation of 660 nm (a). ESA_1 and ESA_2 originate mainly from the BPY excitation, as can be seen in Fig. S5c. In contrast to the excitation of RHO-BPY-OH with 565 nm pulses, an excitation energy transfer (EET) is not observable, which can also be deduced from the missing time component in the LDM (b). A small fraction of RHO might have been excited due to a slight spectral overlap of the RHO absorption and the excitation pulses, leading to the weak GSB_2 signal. The transients shown in (c) and (d) underline that the excitation of RHO-BPY-OH with 660 nm pulses leads to a locally excited state of the BPY moiety.

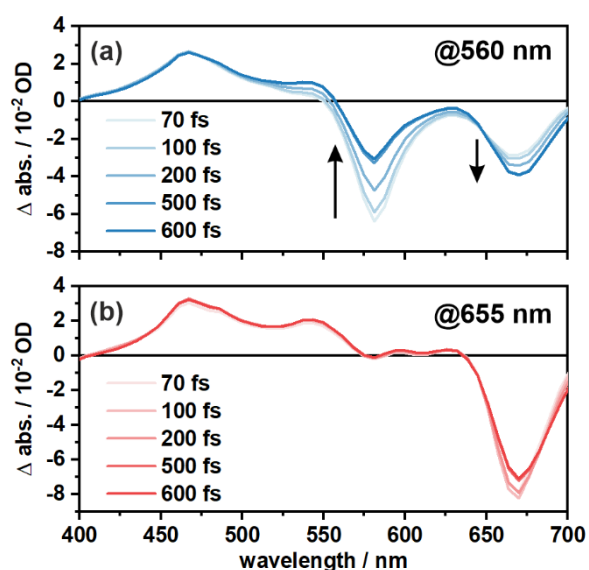


Figure S7. Transient spectra of RHO-BPY-OH at different delay times. Excitation with 560 nm pulses (a) and excitation with 655 nm pulses (b). The arrows in (a) indicate the ET from the RHO part to BPY. This is not observed after direct excitation of BPY.

Theoretical investigation of RHO-BPY-OH

Electronic structure calculations

All ground state structures have been optimized using DFT with the B3LYP functional and 6-31G* basis as included in the *GAUSSIAN 16* program package.⁹ Solvent effects of methanol were included using the polarizable continuum model (PCM).^{10,11} Geometry optimizations using other functionals (e. g. BHandHLYP, CAM-B3LYP or wB97xD) partially yielded implausible geometries for the rhodamine species where the carboxylate anion would form a lactone type ring with the π -system of the rhodamine (see also the discussion below). This would then lead to a loss of the planarity of the π -system, which made the B3LYP/6-31G* combination the overall best method for the geometry optimization. The obtained minimum structures were confirmed using the Hessian.

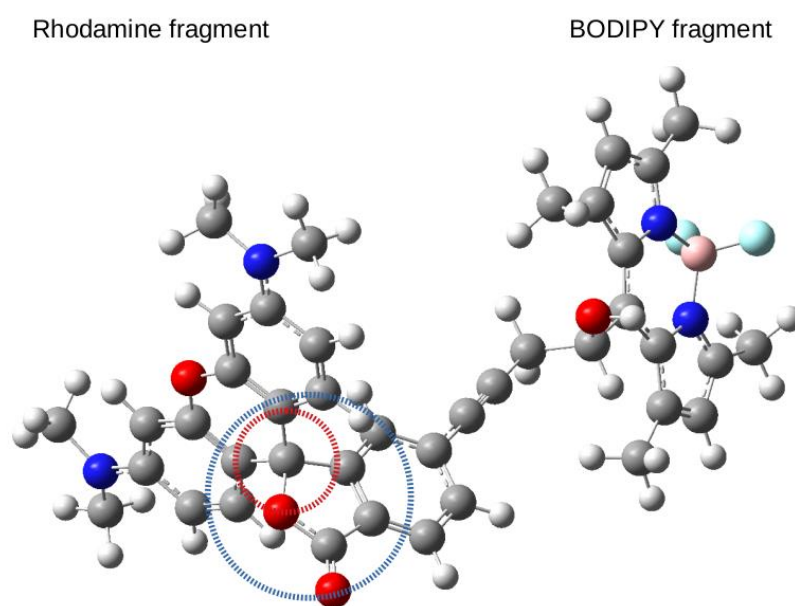


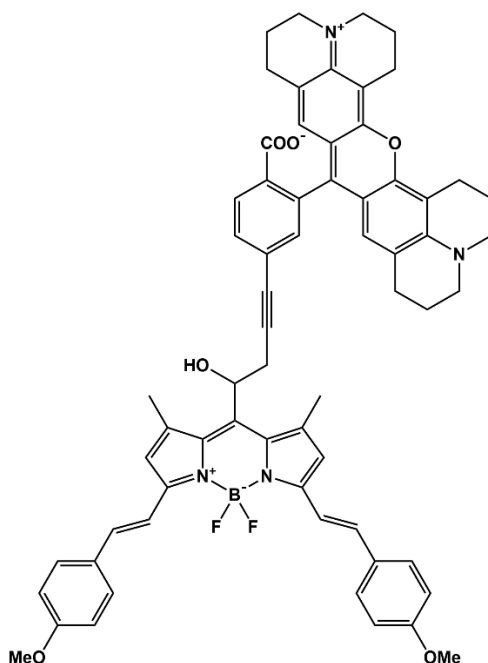
Figure S8: The rhodamine species optimized with the BHandHLYP functional and the 6-31G* basis where the carboxylate anion forms a lactone type ring with the π -system of the rhodamine.

The excited state analysis for the RHO-BPY-OH system as well as the model system (M) Rho1-BPY1-OH were performed using TD-DFT with multiple different functional and basis set combinations (see Tab. S2 and S3). Overall CAM-B3LYP, wB97XD, BHandHLYP as well as M06-2X showed a correct state ordering in which the BODIPY centered state is the S_1 state, the rhodamine centered state is the S_2 state followed by another rhodamine centered state as well as consistent energies for these states. The other tested methods

(B3LYP, PBE0 and M05) either yielded an incorrect state ordering or strongly deviating states energies. CAM-B3LYP was chosen for the analysis due to overall reasonable performance as well as availability in the other relevant program packages (DALTON and Q-CHEM). The basis set size seems to have only a small impact on the energies, making 6-31G* feasible for the analysis. Quadratic response calculations have been performed using the DALTON program package.¹²

Table S2. Benchmark of the RHO-BPY-OH dyad including the three excited states of interest, namely the lowest excited state located on the BPY fragment and the two excited states located on the RHO fragment that correspond to the desired orbital transitions, one of which is the two-photon active state. Listed are the excitation energy in eV and nm and the respective oscillator strength (*f*).

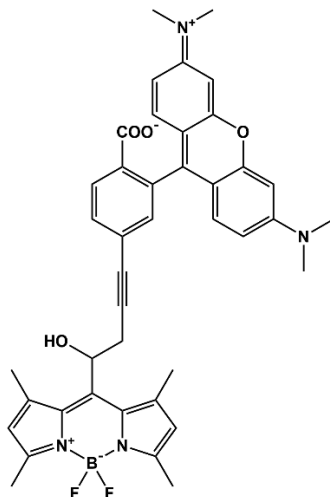
RHO-BPY-OH



Functional	Basis set	BPY-state	Energy [eV]	Energy [nm]	f	RHO-state	Energy [eV]	Energy [nm]	f	RHO-2P-state	Energy [eV]	Energy [nm]	f
CAM-B3LYP	6-31G*	1	2.1413	579.02	1.1307	2	2.8624	433.14	1.0555	4	3.5065	353.58	0.0788
BHandHLYP	6-31G*	1	2.1612	573.68	1.1829	2	2.9565	419.36	1.1180	4	3.6239	342.13	0
B3LYP	6-31G*	1	1.9720	628.72	1.0632	5	2.6313	471.19	0.8654	7	2.8039	442.19	0.1095
wB97XD	6-31G*	1	2.1635	573.08	1.1340	2	2.8810	430.35	1.0591	3	3.5034	353.90	0.7288
PBE0	6-31G*	1	2.0136	615.73	1.0918	4	2.6828	462.15	0.9242	7	2.9691	417.58	0.1614
M05	6-31G*	1	1.9975	620.69	1.0826	3	2.7246	455.05	0.9113	7	2.9942	414.08	0.1472
M06-2X	6-31G*	1	2.1301	582.07	1.1143	2	2.8059	441.88	1.0790	5	3.5372	350.51	0.0523
CAM-B3LYP	svp	1	2.1396	579.47	1.1421	2	2.8436	436.01	1.0542	4	3.4921	355.04	0.0628
CAM-B3LYP	def2-tzvp	1	2.0917	592.74	1.1157	2	2.7916	444.14	1.0600	4	3.5209	352.14	0.0035

Table S3. Benchmark of the model system (M) Rho1-BPY1-OH including the three excited states of interest, namely the lowest excited state located on the BPY1 fragment and the two excited states located on the Rho1 fragment that correspond to the desired orbital transitions, one of which is the two-photon active state. Listed are the excitation energy in eV and nm and the respective oscillator strength (*f*).

Model System (Rho1-BPY1-OH)



Functional	Basis set	BPY1-state	Energy [eV]	Energy [nm]	f	Rho1-state	Energy [eV]	Energy [nm]	f	Rho1-2P-state	Energy [eV]	Energy [nm]	f
CAM-B3LYP	6-31G*	1	2.8611	433.35	0.5711	2	3.0616	404.97	0.9615	3	3.5648	347.80	0.3422
BHandHLYP	6-31G*	1	2.9266	423.64	0.6078	2	3.1652	391.71	1.0261	3	3.8876	318.92	0.3615
B3LYP	6-31G*	3	2.8779	430.82	0.4587	2	2.7661	448.22	0.7293	5	2.9022	427.21	0.1448
wB97XD	6-31G*	1	2.8606	433.42	0.5798	2	3.0846	401.95	0.9651	3	3.5658	347.70	0.3409
PBE0	6-31G*	3	2.8988	427.70	0.5527	1	2.8291	438.24	0.7852	4	3.0844	401.97	0.1679
M05	6-31G*	1	2.8479	435.35	0.5210	2	2.8934	428.51	0.8394	4	3.1059	399.19	0.0958
M06-2X	6-31G*	1	2.8460	435.65	0.5575	2	2.9919	414.41	0.9921	3	3.5798	346.34	0.3477
CAM-B3LYP	svp	1	2.8609	433.38	0.5892	2	3.0408	407.74	0.9620	3	3.5491	349.34	0.3301
CAM-B3LYP	def2-tzvp	1	2.7917	444.12	0.5782	2	2.9865	415.15	0.9872	3	3.7140	333.83	0.3200

Excited state analysis of BODIPY derivatives

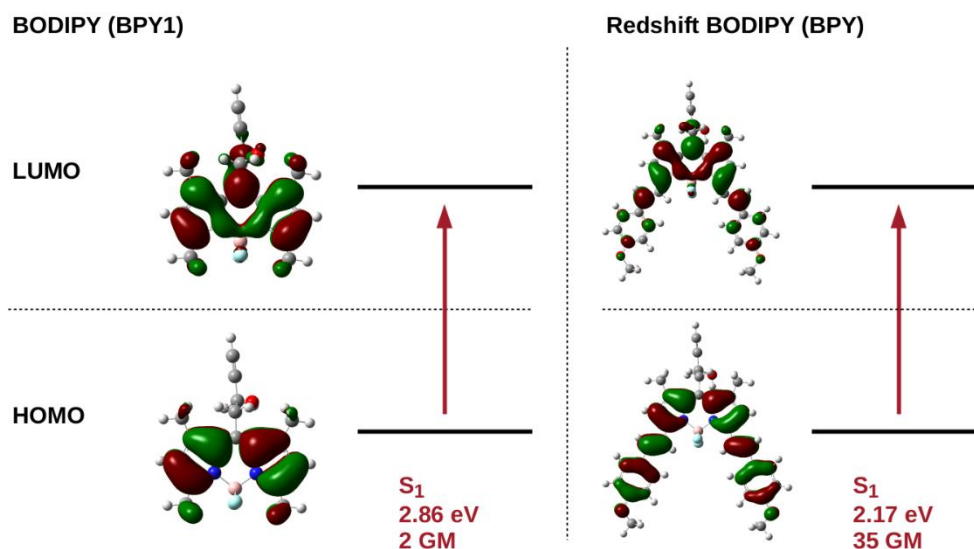


Figure S9: Relevant frontier molecular orbital transition, excitation energies and two-photon absorption cross-sections for the first excited electronic state in case of the unsubstituted BODIPY(BPY1) and the redshifted BODIPY(BPY) compound with *ortho*-methoxyphenyl substituents at CAM-B3LYP/6-31G* level in methanol.

Excited state analysis of Rhodamine derivatives

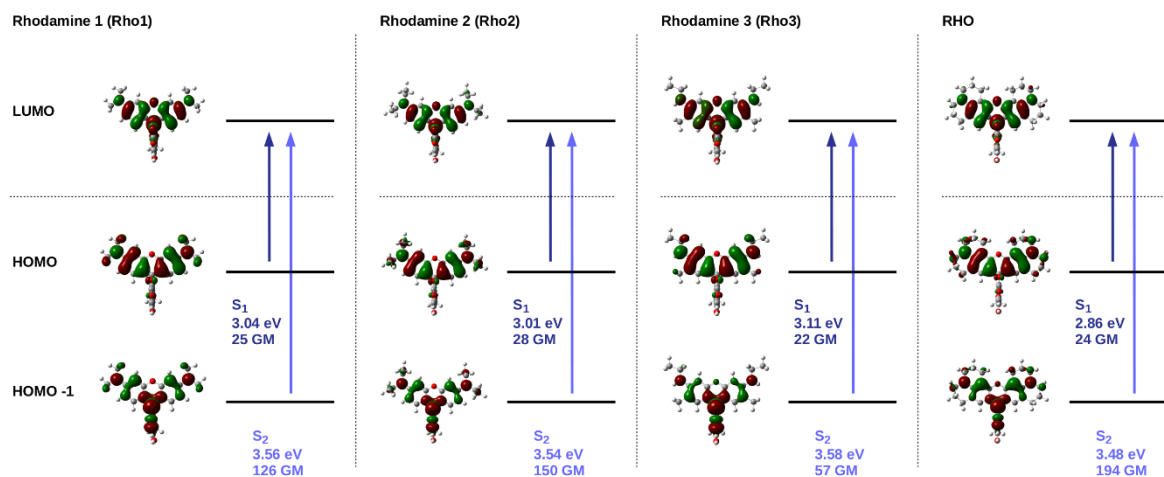


Figure S10: Relevant frontier molecular orbital transitions, excitation energies and two-photon absorption cross-sections of the first two excited electronic states of the four Rhodamine compounds with different substitution pattern Rho1, Rho2, Rho3, and RHO at CAM-B3LYP/6-31G* level in methanol.

Excited state analysis of RHO-BPY-OH

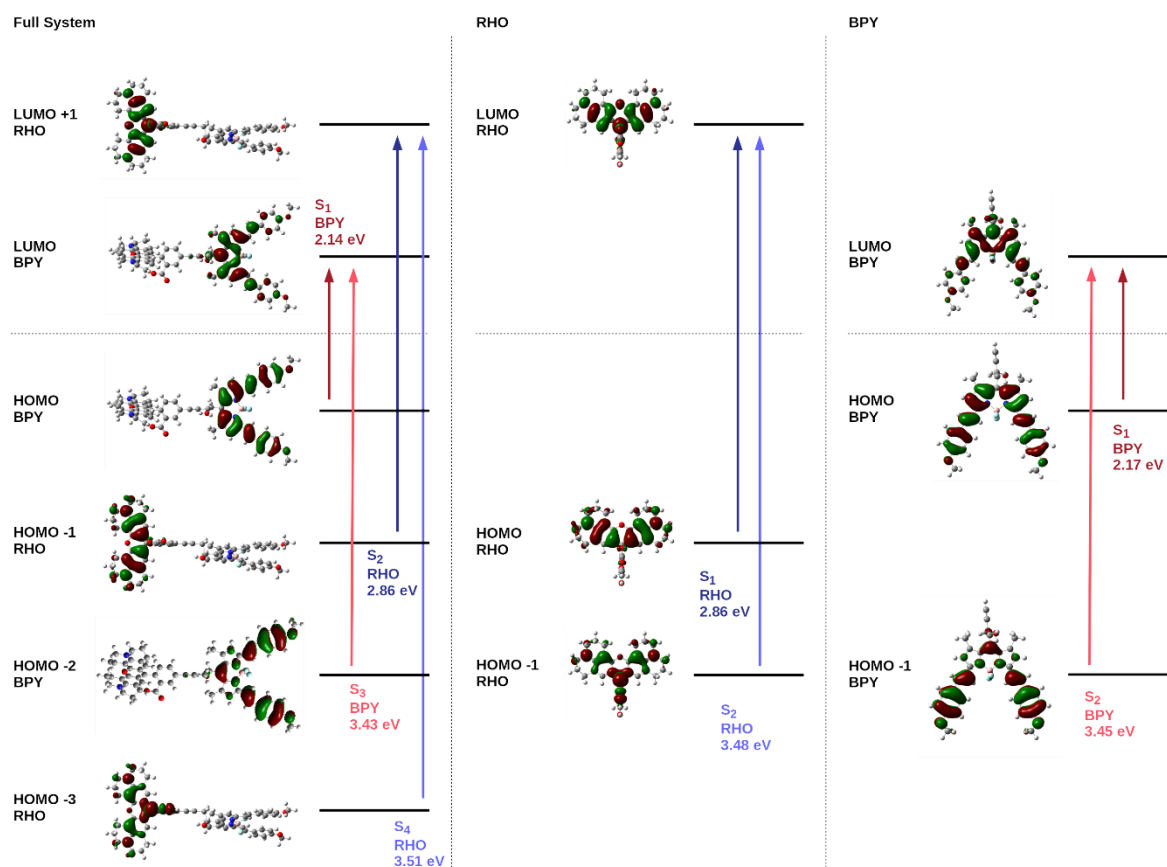


Figure S11: Relevant frontier molecular orbital transitions, excitation energies and two-photon absorption cross-sections of the first four excited electronic states of RHO-BPY-OH in comparison to the respective properties of the individual fragments BPY and RHO at CAM-B3LYP/6-31G* level in methanol.

As explained in the main text, the S₁ state (localized on the BPY fragment) and the S₂ and S₄ states (both localized on the RHO fragment) play a key role in the dynamics. For completeness, we also comment here on the S₃ state, that is included for RHO-BPY-OH in Figure S11. This state is localized on the BPY moiety and does not exhibit any significant contribution of rhodamine centered orbital transitions; therefore, this state is not involved in the initial internal conversion (IC) step on the RHO moiety, and it is also not involved in the ensuing excitation energy transfer (EET). Therefore, the S₃ state can be assumed to be irrelevant for the observed dynamics.

Excited state analysis of Rho1-BPY1-OH

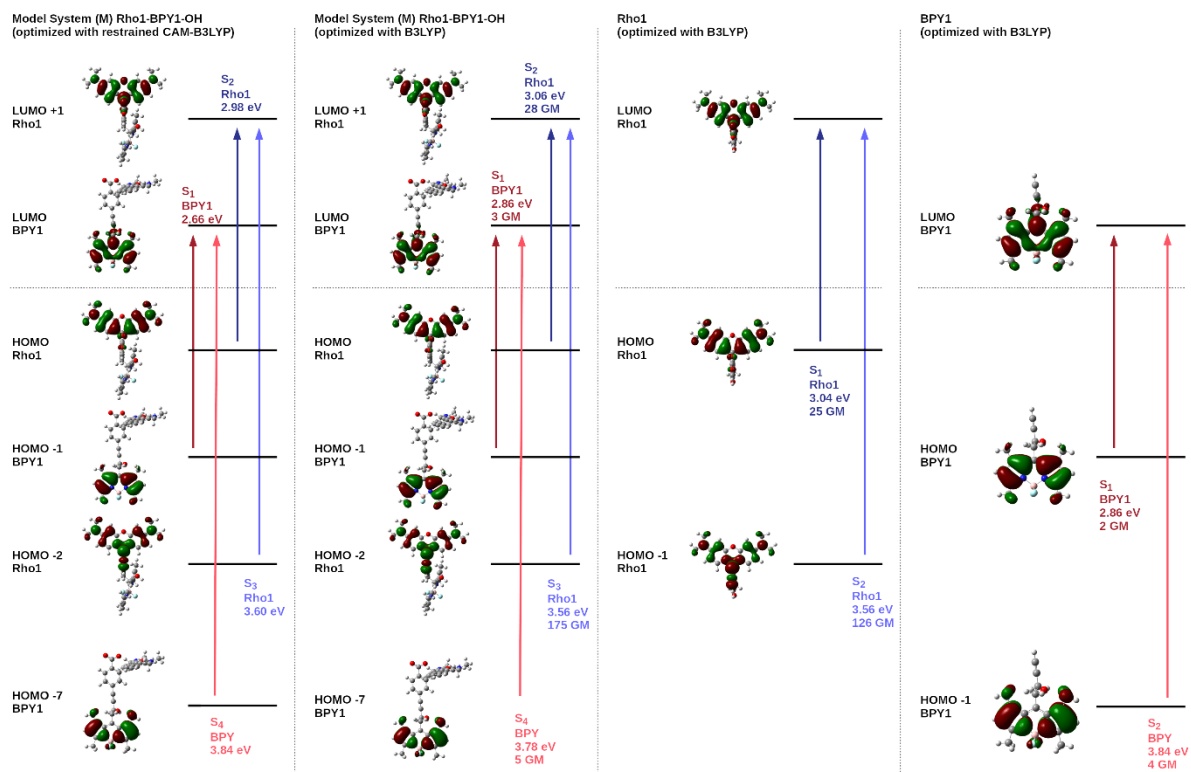


Figure S12: Relevant frontier molecular orbital transitions, excitation energies and two-photon absorption cross-sections of the first four excited electronic states of the model dyad (M) Rho1-BPY1-OH in comparison to the respective properties of the individual fragments BPY1 and Rho1 at CAM-B3LYP/6-31G* level in methanol. For simplicity, the states are marked as S_n (rather than $S_n^{(M)}$) in the figure. On the left-hand side, CAM-B3LYP calculations for two reference geometries are compared: First, the ground state geometry optimized with CAM-B3LYP using the constraint shown in Figure S14, and second, the reference geometry optimized with B3LYP; in this geometry, lactone formation is inhibited. As can be inferred from the figure, the excitation energies are reasonably similar for these geometries, with deviations up to 0.2 eV.

For the model system Rho1-BPY1-OH, two ground-state reference geometries are shown in Figure S12, i.e., the B3LYP optimized geometry (as in the case of the RHO-BPY-OH system) and a constrained CAM-B3LYP optimized geometry. The latter geometry is required in order to carry out the vibrational analysis for the quantum dynamical calculations addressed below. The CAM-B3LYP reference geometry is illustrated in Figure S14, where it is shown that the constraint impedes formation of a lactone type structure (see also Figure S8). As can be inferred from Figure S12, good agreement is obtained for CAM-B3LYP excitation energies based on the B3LYP optimized geometry and the constrained CAM-B3LYP optimized geometry for the model system Rho1-BPY1-OH.

The BPY centered S_3 state of the RHO-BPY-OH system that was briefly discussed above, corresponds to the BPY1 centered $S_4^{(M)}$ state in the model system Rho1-BPY1-OH (Figure S12). Again, this state is not going to play an active role since it is not involved in the IC and EET steps of the process.

An explicit comparison between the excited states of RHO-BPY-OH and the model system Rho1-BPY1-OH is shown in Figure S13. From this it becomes obvious that the orbital transitions for the two systems are in general very similar; the main difference being a stronger energetic shift of the BPY/BPY1 centered states which leads to a switch of the S_3/S_4 state sequence in the model system. Thus, the BPY centered state S_3 is equivalent to the $S_4^{(M)}$ state while the RHO centered state S_4 is equivalent to the $S_3^{(M)}$ state.

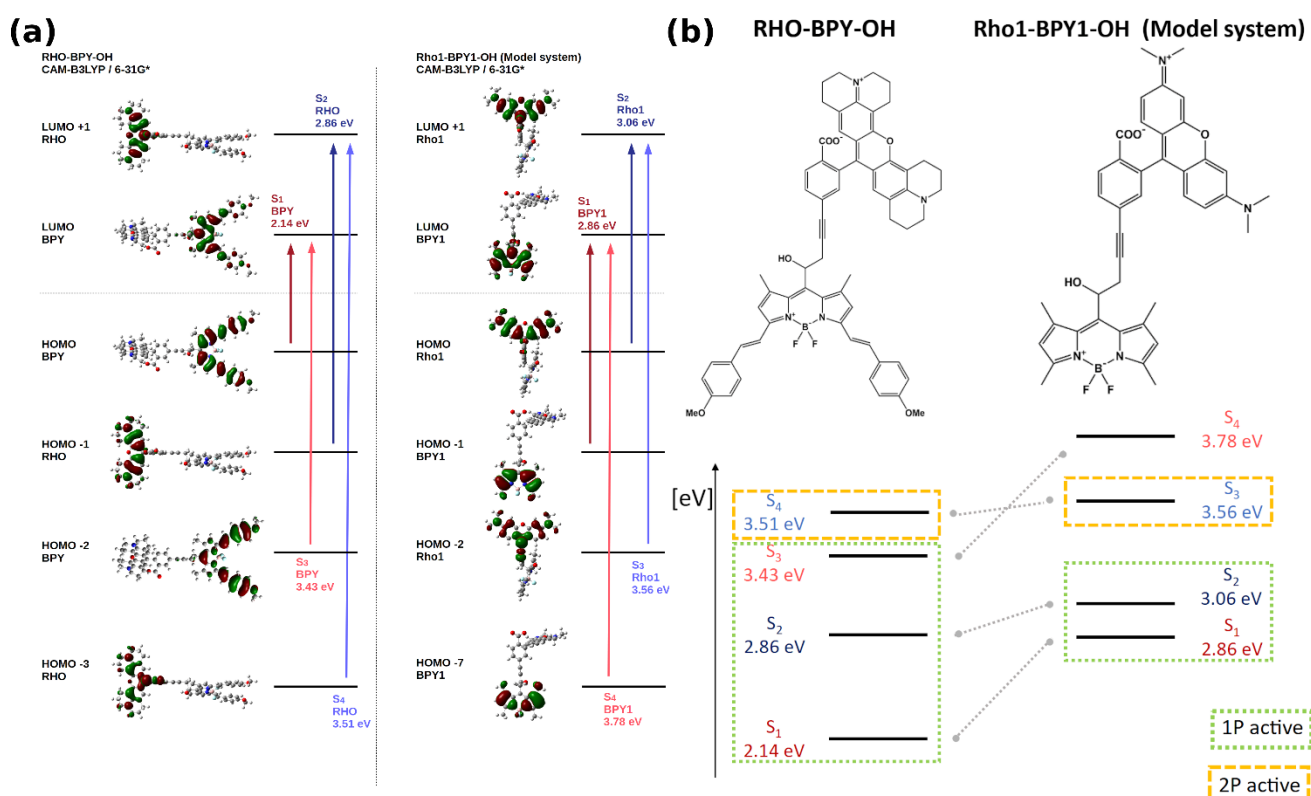


Figure S13: Comparison between the electronic structure and excited state composition of RHO-BPY-OH and the model system Rho1-BPY1-OH (a). A diagrammatic representation correlating the respective states is shown in (b).

As mentioned above and confirmed by Figure S8 an unconstrained optimization with functionals like CAM-B3LYP or BHandHLYP yields a lactone type structure. For the quantum dynamical analysis, the optimized ground state geometry as well as the excited state gradients need to be calculated with the same method. For this reason all results

connected to the quantum dynamical analysis are obtained using a constrained, planar CAM-B3LYP ground state geometry. The constraint includes three frozen atoms that connect the *ortho*-carboxyphenyl with the xanthene fragment of Rho1 so that the dihedral angle between these two moieties is set to 90° and the formation of a lactone type five-membered ring is not possible (Figure S14).

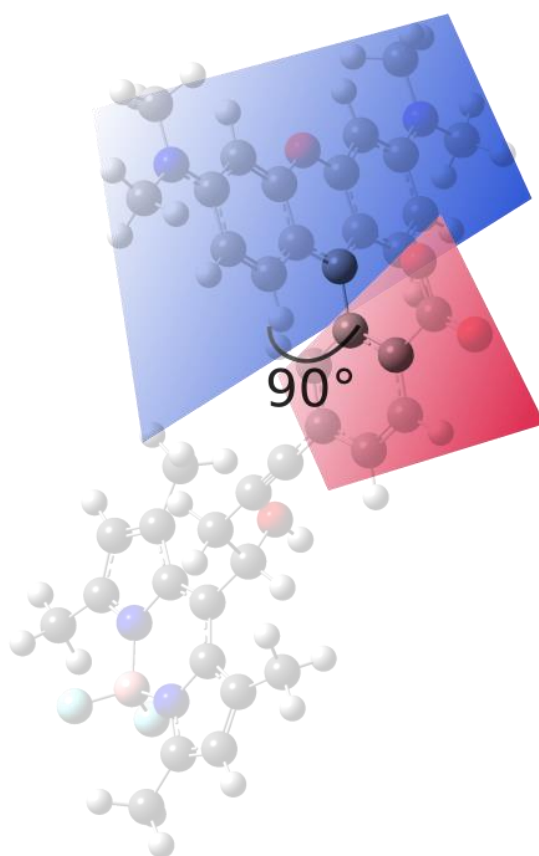


Figure S14: Illustration of the constraint that is used for the CAM-B3LYP ground state optimization of Rho1-BPY1-OH showing the three atoms that are frozen to prevent the formation of a lactone type structure. This imposes a 90° dihedral angle between the xanthene fragment of the rhodamine and its *ortho*-carboxyphenyl substituent.

This structure contains $N = 267$ normal modes including one imaginary mode caused by the constraint on the carboxylate group. The imaginary mode is excluded from the quantum dynamical analysis.

Electronic coupling via ideal dipole approximation and transition density cubes

When calculating an electronic coupling between a donor and acceptor fragment with no orbital overlap as a Coulombic interaction the ideal dipole approximation (IDA) can be used. In this case, the Coulombic interaction is calculated based on the interaction between the transition dipole vector of the donor fragment and the transition dipole vector of the acceptor fragment and reads

$$V_{DA} = \frac{\vec{\mu}_D \vec{\mu}_A}{R_{DA}^3} - \frac{3(\vec{\mu}_D \vec{R}_{DA})(\vec{\mu}_A \vec{R}_{DA})}{R_{DA}^5} \quad (3)$$

Here $\vec{\mu}_D$ and $\vec{\mu}_A$ denote the transition dipoles of the donor and the acceptor and \vec{R}_{DA} and R_{DA} are the vector and distance between the centers of mass of the donor and acceptor fragment.

A more accurate way to compute the Coulombic interaction is using the transition density cube method (TDC). In general, the transition density of a molecule N is defined as

$$\rho_N^{\text{el}}(\vec{r}_n) = \Psi_{N_g}(\vec{r}_n) \Psi_{N_e}^*(\vec{r}_n) \quad (4)$$

where Ψ_{N_g} is the electronic ground state of the molecule, Ψ_{N_e} the excited state and \vec{r}_n are the respective electron coordinates, with $N = A$ ($n = a$) referring to the acceptor fragment and $N = D$ ($n = d$) to the donor fragment. In this case the coupling reads¹³⁻¹⁵

$$V_{DA} = \iint \rho_D^{\text{el}}(\vec{r}_d) \frac{1}{|\vec{r}_d - \vec{r}_a|} \rho_A^{\text{el}}(\vec{r}_a) d\vec{r}_d d\vec{r}_a \quad (5)$$

with the electron coordinates \vec{r}_d and \vec{r}_a . The transition density can then be defined on a three-dimensional grid where the elements δ_x , δ_y and δ_z are the step size in the respective Cartesian coordinate axis. The grid is chosen according to the extent of the molecule in the direction of the respective axis plus an additional step δ_x , δ_y and δ_z to account for edge effects. In this specific case 84 elements in x direction, 63 elements in y direction and 52 elements in z direction with an equidistant spacing of $\delta_x = \delta_y = \delta_z = 0.3 \text{ \AA}$ are taken into account, which gives a total of 275184 cubes.

The Coulombic coupling calculation based on the transition density formalism by McWeeny¹⁴ can be adapted for the transition density cubes¹⁵

$$V_{\text{coul}} \cong \sum_{i,j} \frac{\rho_A^{\text{el}}(i) \rho_D^{\text{el}}(j)}{4\pi\epsilon_0 r_{ij}} \quad (6)$$

Here, $\rho_A^{\text{el}}(i)$ and $\rho_D^{\text{el}}(j)$ are the TDC elements i and j for the donor and the acceptor moiety and r_{ij} is the respective distance. The transition dipoles can be recovered from the TDC as the first moment of the transition densities.

TDCs have been calculated using the Q-CHEM program package.¹⁶ Electronic couplings have been calculated using Eq. (6) with an in-house program written in C++. For the model system (M) Rho1-BPY1-OH using the CAM-B3LYP functional and 6-31G* basis set a Coulombic EET coupling of 0.00091 Hartree (0.024 eV) was obtained. The respective electronic coupling obtained by the ideal dipole approximation was 0.00041 Hartree (0.011 eV) for comparison.

Initial condition for quantum dynamical simulations

The initial condition for the quantum dynamical calculation is chosen according to the excitation scheme as depicted in Figure 3b of the main text. As the initial excitation to the two-photon active S_4 state (in case of RHO-BPY-OH) and the S_3^M state (in case of the model system Rho1-BPY1-OH) likely undergoes ultrafast IC to the S_2/S_2^M state within the RHO/Rho1 fragment, the latter is chosen as initial condition for the quantum dynamics. Due to the natural localization of the respective excited states, this means that all density is located on the Rho1 fragment in the beginning. This locally excited state can be identified with a “diabatic” donor state LE^D which subsequently undergoes EET to a localized acceptor state LE^A .

Linear Vibronic Coupling (LVC) model

The excited state potentials are constructed within a shifted harmonic oscillator model, i.e. the Linear Vibronic Coupling (LVC) model. Thus, the diagonal excited state potentials

of all states along the mass- and frequency weighted normal coordinate q_i can be expressed as

$$\begin{aligned}
 V_\alpha(q_i) &= \frac{1}{2} \omega_i (q_i - q_{i,0}^{(\alpha)})^2 + \Delta E \\
 &= \frac{1}{2} \omega_i q_i^2 + \kappa_i^{(\alpha)} q_i + d_i + \Delta E
 \end{aligned}
 \tag{7}$$

where ω_i is the normal mode frequency, $q_{i,0}^{(\alpha)}$ the shifted minimum of the excited state potential and ΔE the vertical energy offset. The vibronic couplings $\kappa_i^{(\alpha)} = -\omega_i q_{i,0}^{(\alpha)}$ can be computed by projecting the cartesian gradient of the respective state of interest onto the molecular normal modes

$$\kappa_i^{(\alpha)} = \left(\frac{\partial V_\alpha(q)}{\partial q_i} \right)_{q_0}
 \tag{8}$$

Spectral densities

The collection of vibronic couplings $\kappa_i^{(\alpha)}$ defines state specific spectral densities.¹⁷

$$J_\alpha(\omega) = \frac{\pi}{2} \sum_{i=1}^N \kappa_i^{(\alpha)2} \delta(\omega - \omega_i)
 \tag{9}$$

These are subsequently convoluted with a Lorentzian broadening with $\tilde{\Delta} = \Delta * 0.2$ where Δ is the root mean square of the frequency differences. In order to calculate the spectral densities of the individual fragments all degrees of freedom of the respective other fragment were frozen in the normal mode calculation.

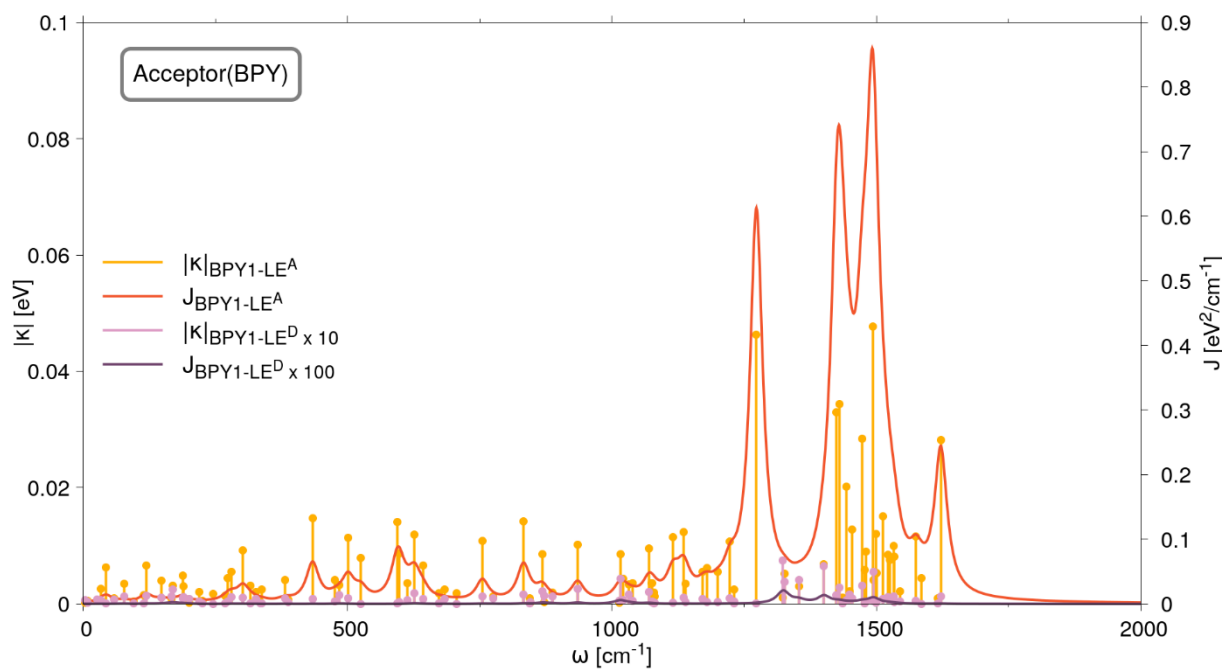


Figure S15: Spectral density J and absolute values of the vibronic couplings $\kappa_i^{(\alpha)}$ between the normal modes located on the acceptor BPY1 fragment and the LE^A state (corresponding to the adiabatic S_1^M state) and LE^D state (corresponding to the adiabatic S_2^M state), whose orbital transitions are naturally located on the BPY1 and Rho1 fragment.

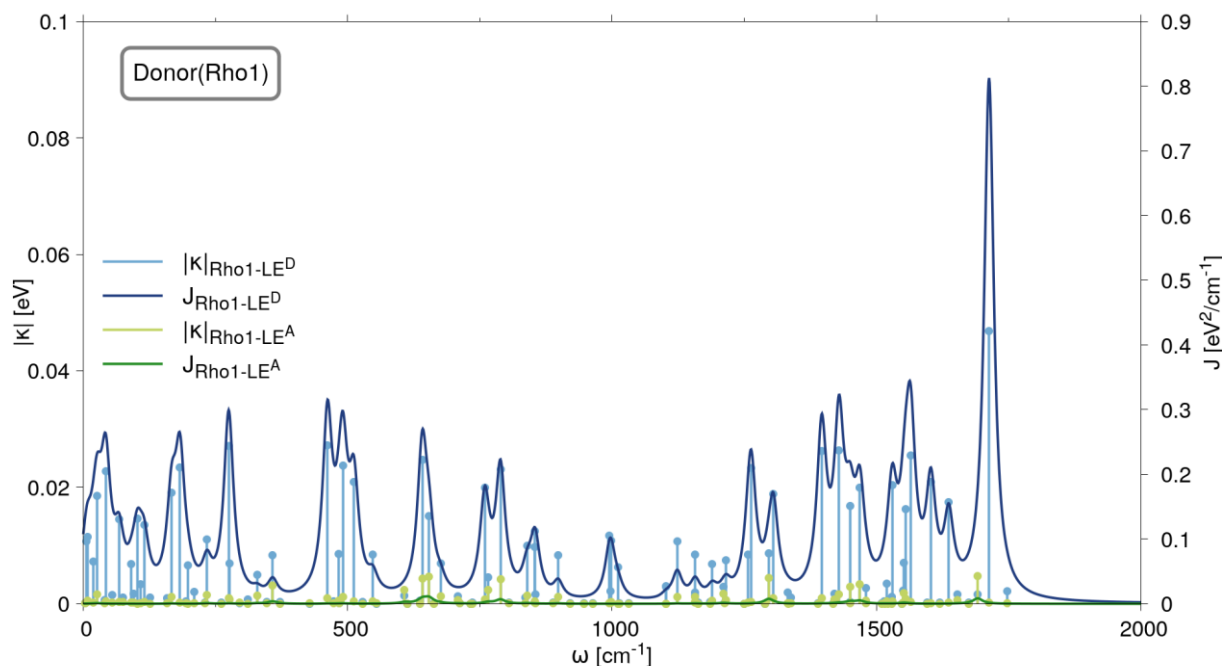


Figure S16: Spectral density J and absolute values of the vibronic couplings $\kappa_i^{(\alpha)}$ between the normal modes located on the donor Rho1 fragment and the LE^A state (corresponding to the adiabatic S_1^M state) and LE^D state (corresponding to the adiabatic S_2^M state), whose orbital transitions are naturally located on the BPY1 and Rho1 fragment.

The imaginary mode due to the ground-state constraint on the CAM-B3LYP calculations, as discussed above, is not included in the spectral density. Also, this mode is not taken into account for any quantum dynamical simulations.

Additionally, the time dependent expectation value of the position operator \hat{q} is depicted in Figure S17 for the first 500 fs alongside the diabatic population and coherence as well as the absolute values of the vibronic couplings between the normal modes located on BPY1 with the LE^A state and the normal modes located on Rho1 with the LE^D state (without the imaginary mode). All modes show a more or less pronounced oscillatory behavior and while the oscillation of the high frequency modes is starting almost directly the low frequency modes show a slight delay. In summary, all modes contribute to the observed energy transfer.

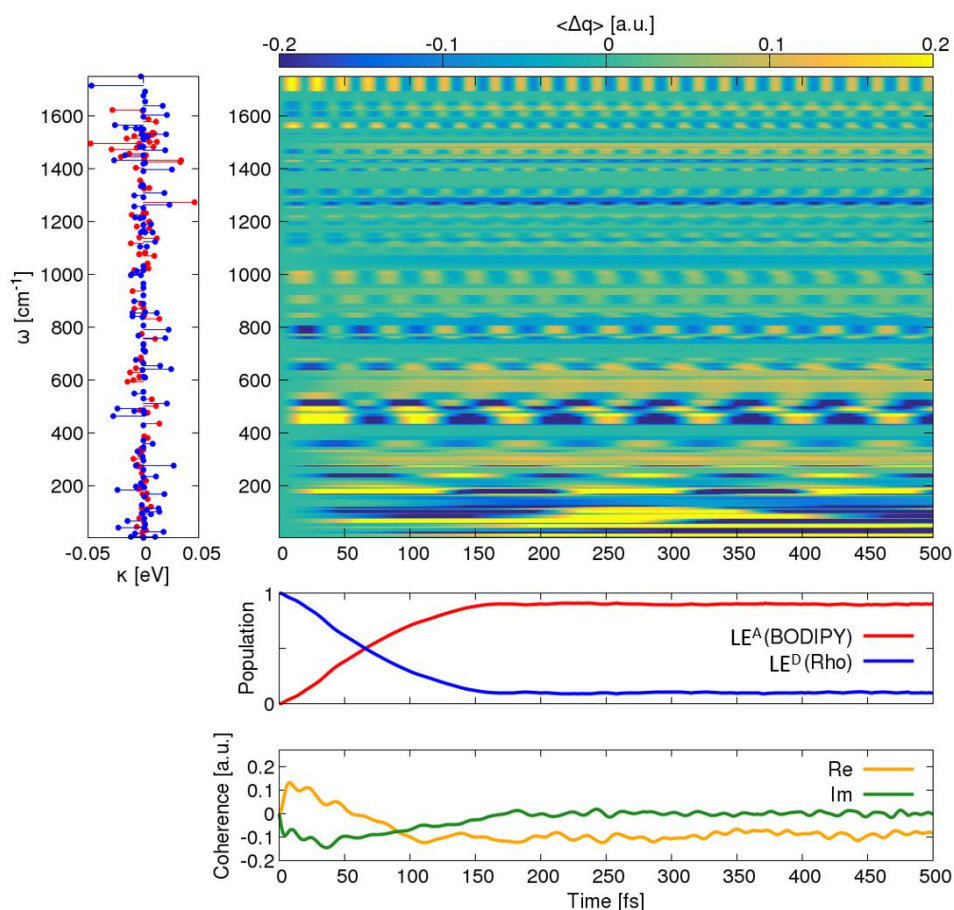
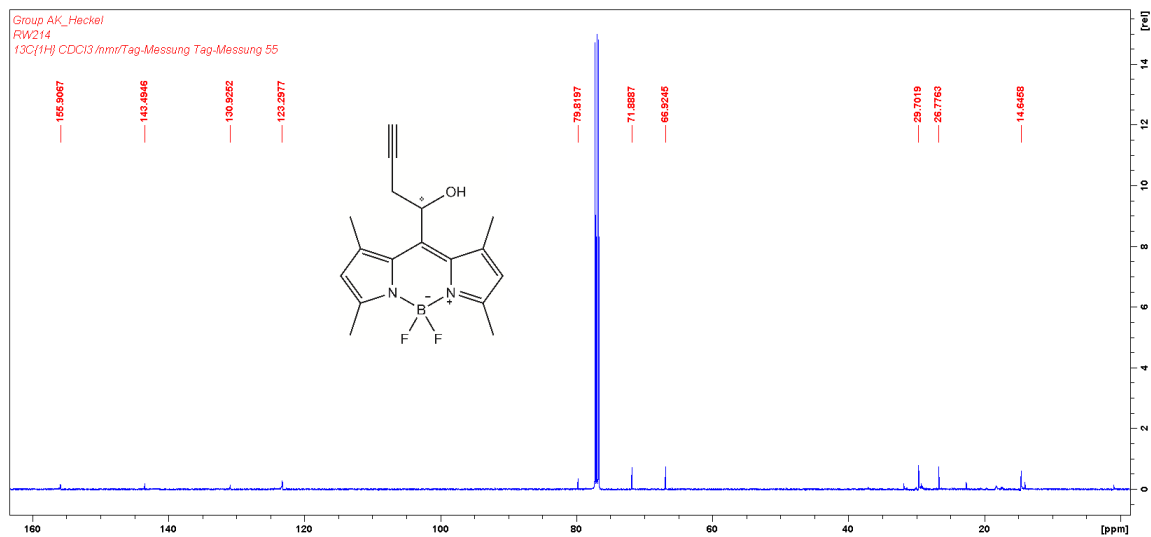
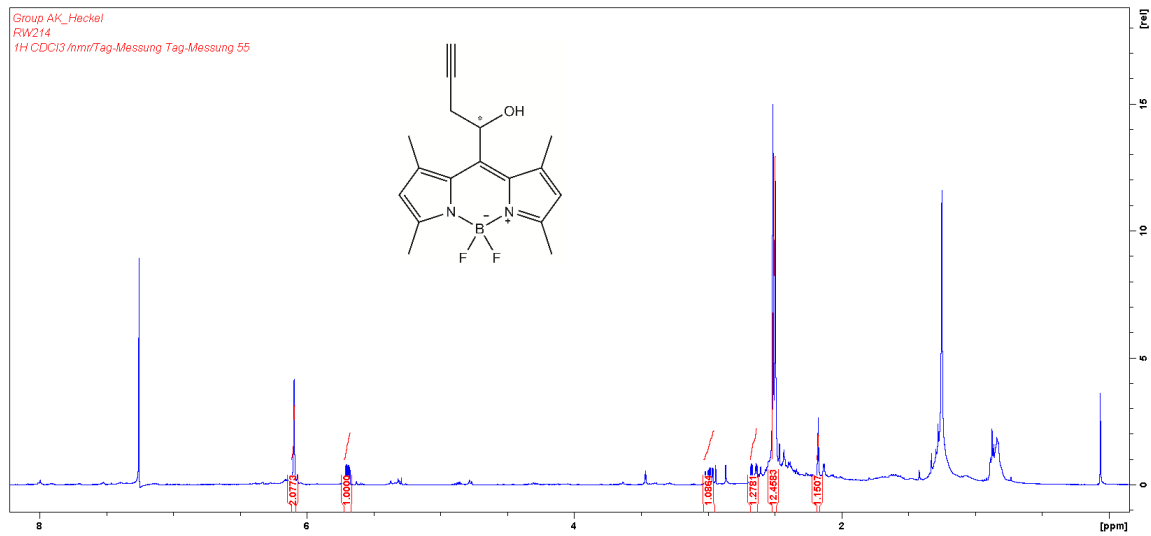


Figure S17: Vibrational map showing the vibronic couplings $\kappa_i^{(\alpha)}$ corresponding to the acceptor (red) and donor state (blue), the time dependent position expectation value and the diabatic population and coherence for the first 300 fs.

NMR- & mass spectra

Compound 3



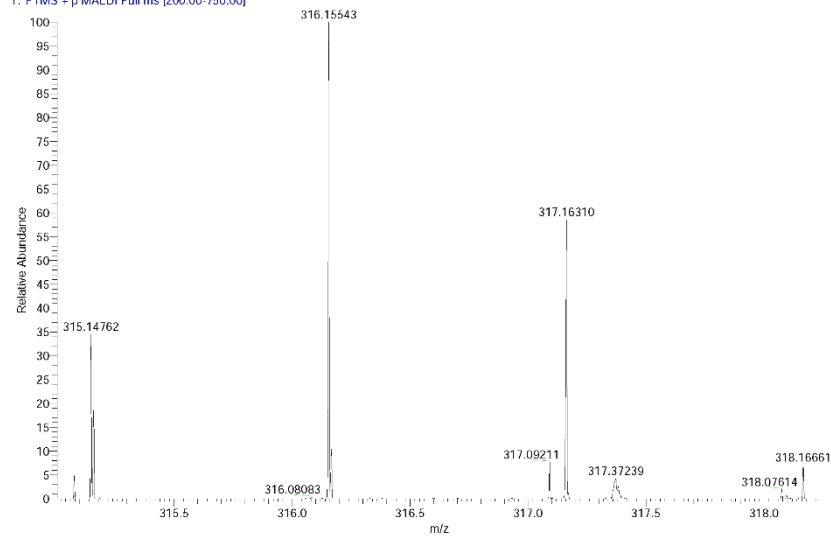
C:\User\...2021116.03.20211BPY-C3_E1

3/16/2021 1:37:22 PM

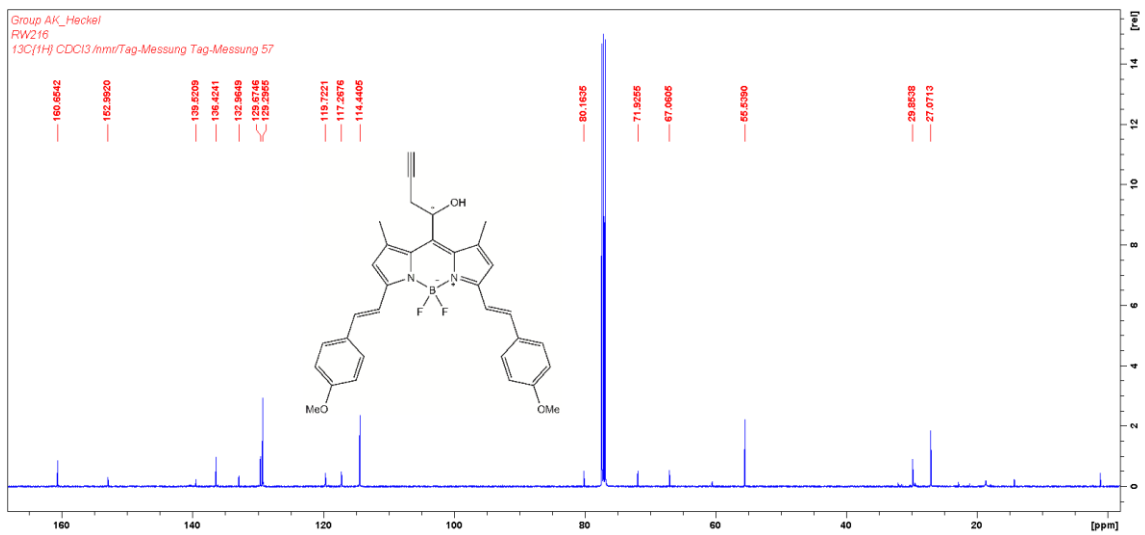
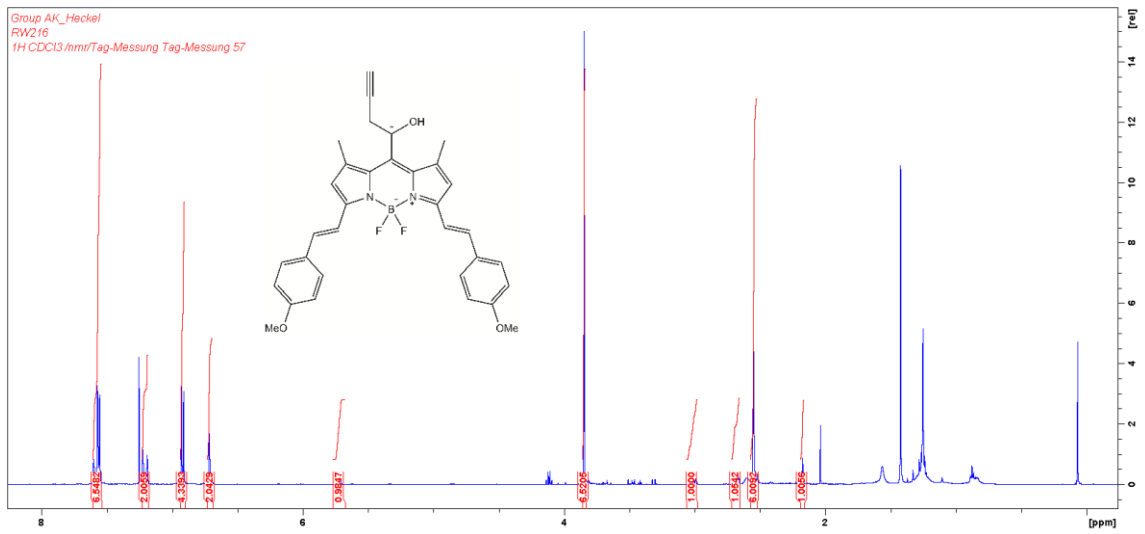
BPY-C3 mit HCCA gemessen.

BPY-C3_E1 #1-12 RT: 0.01-0.51 AV: 12 NL: 3.37E6

T: FTMS - p MALDI Full ms [200.00-750.00]



Compound 4

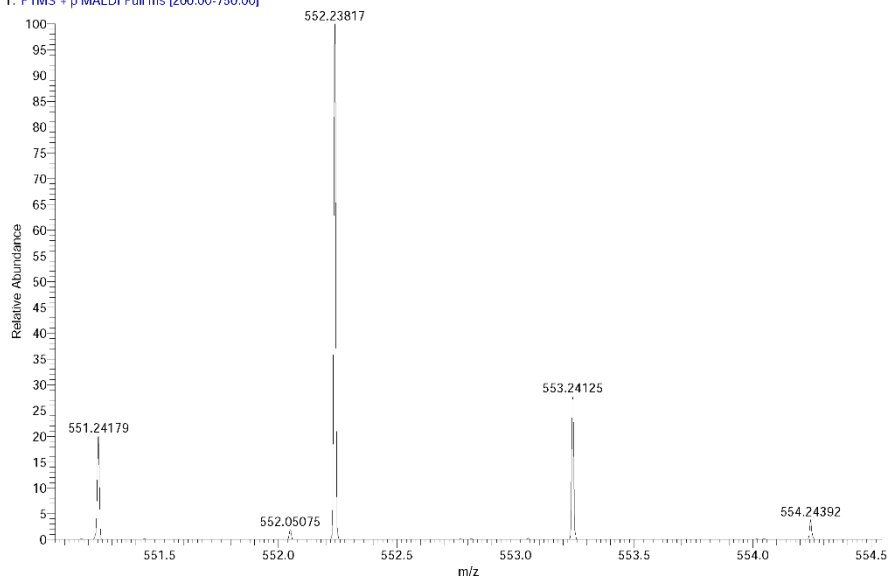


C:\User\...2021\116.03.2021\BPY_Sty_E2

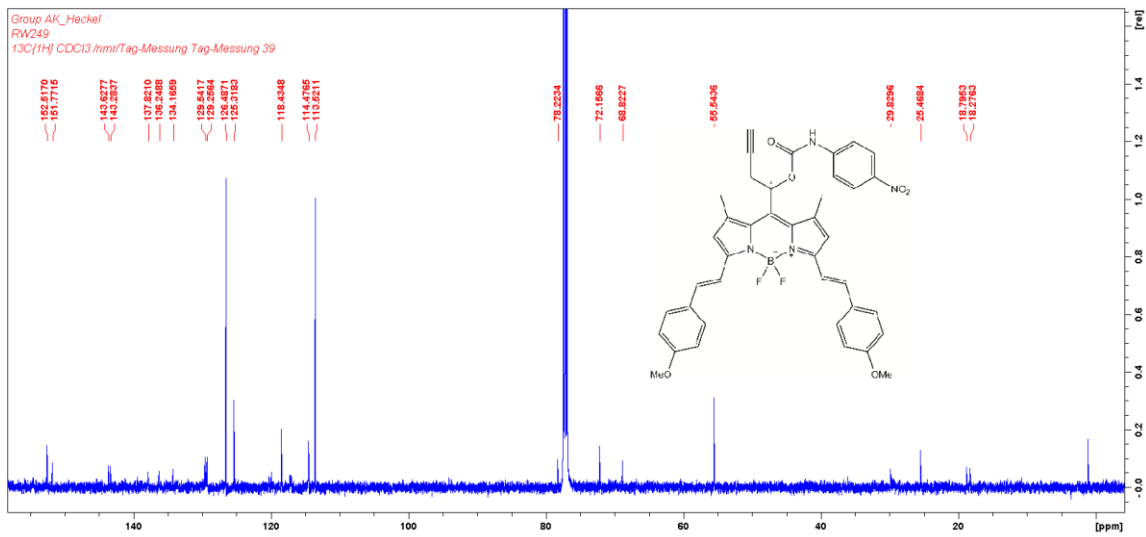
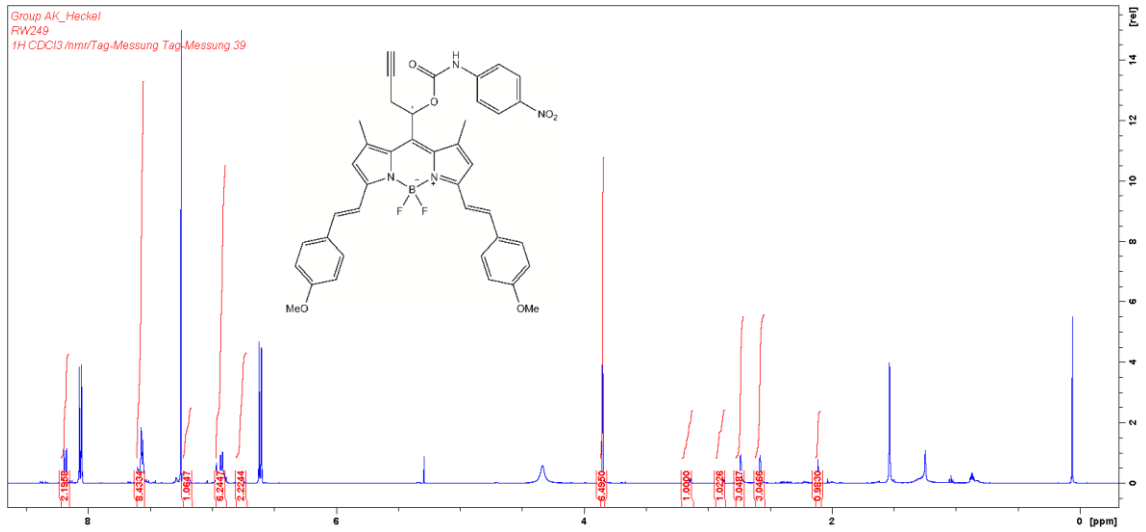
3/16/2021 1:38:35 PM

BPY-Sty mit HCCA gemessen.

BPY-Sty_E2 #1-15 RT: 0.00-0.59 AV: 15 NL: 5.73E6
T: FIMS + p MALDI Full ms [200.00-750.00]



Compound 5

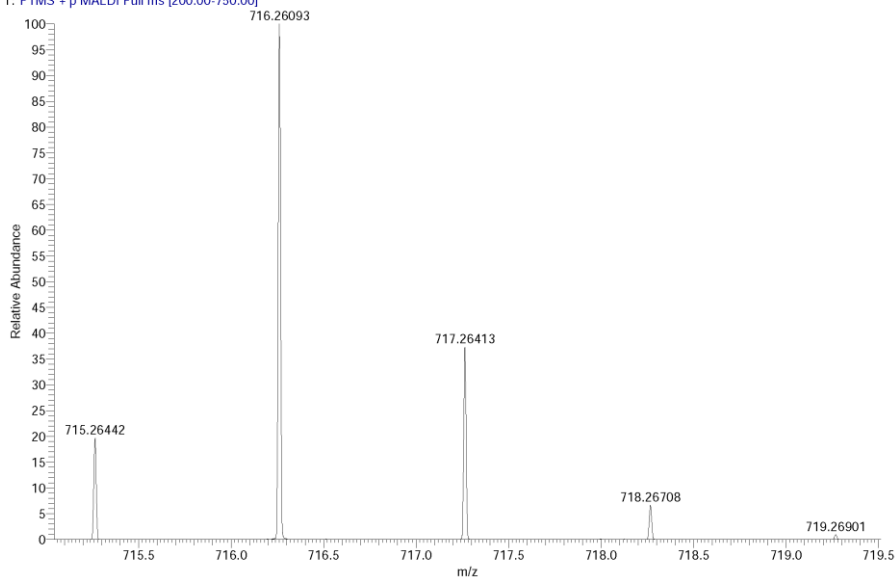


C:\User\... \2021\116.03.2021\BPY-PNA_D9

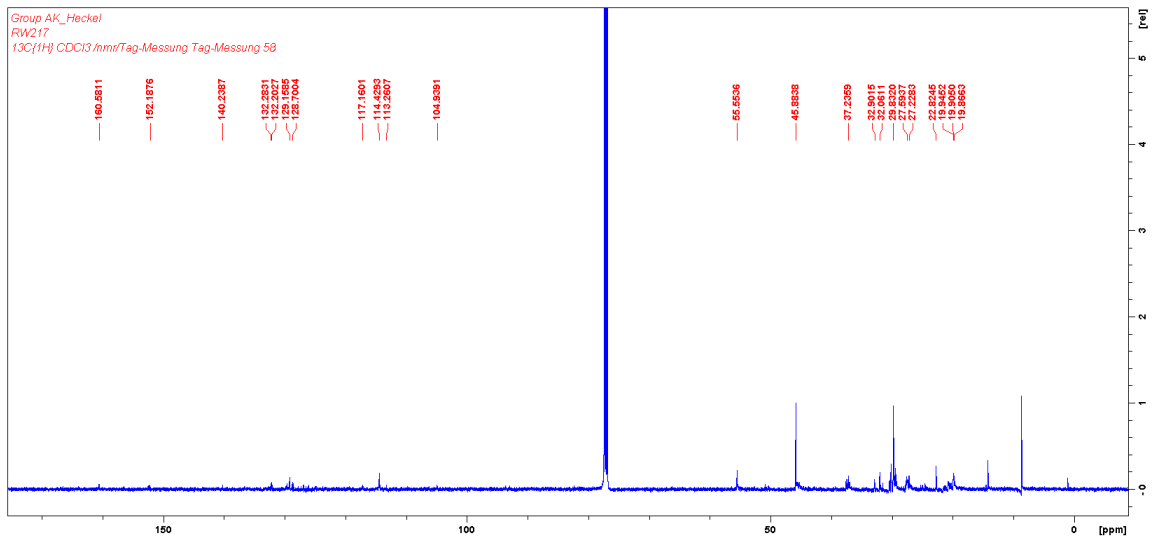
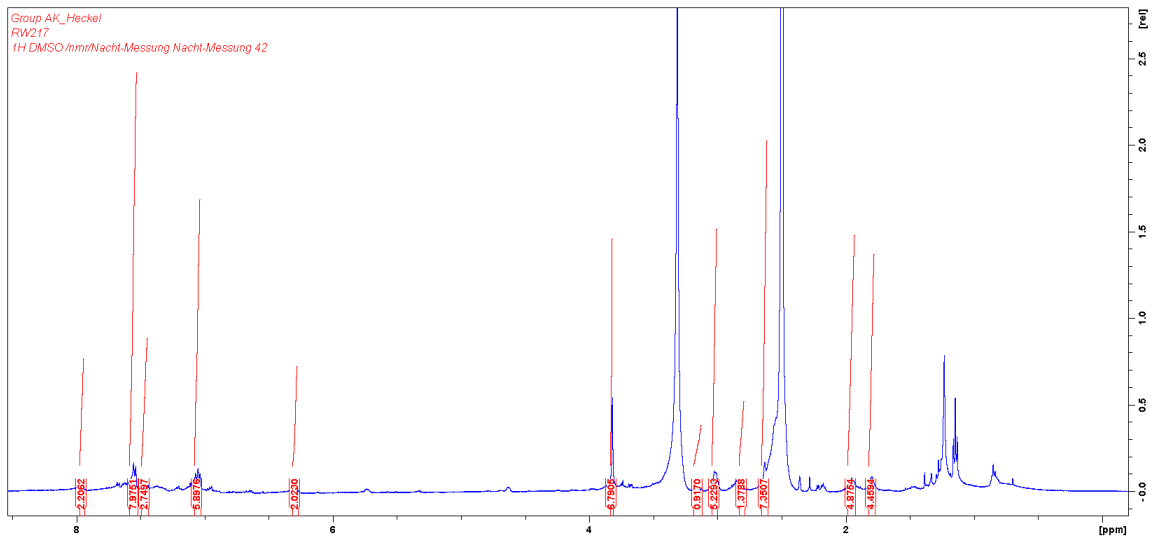
3/16/2021 1:31:33 PM

BPY-PNA mit HCCA gemessen.

BPY-PNA_D9 #1-16 RT: 0.01-0.63 AV: 16 NL: 7.62E6
T: FTMS + p MALDI Full ms [200.00-750.00]



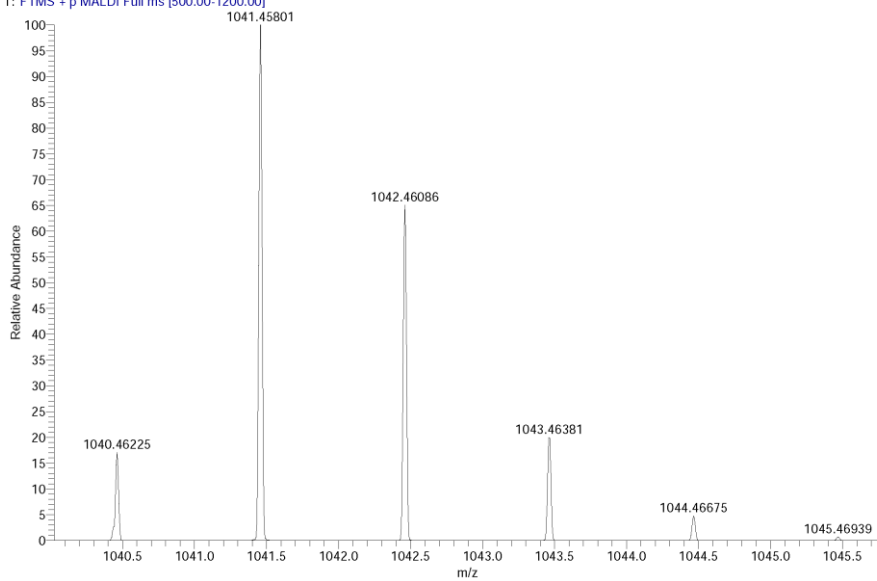
RHO-BPY-OH



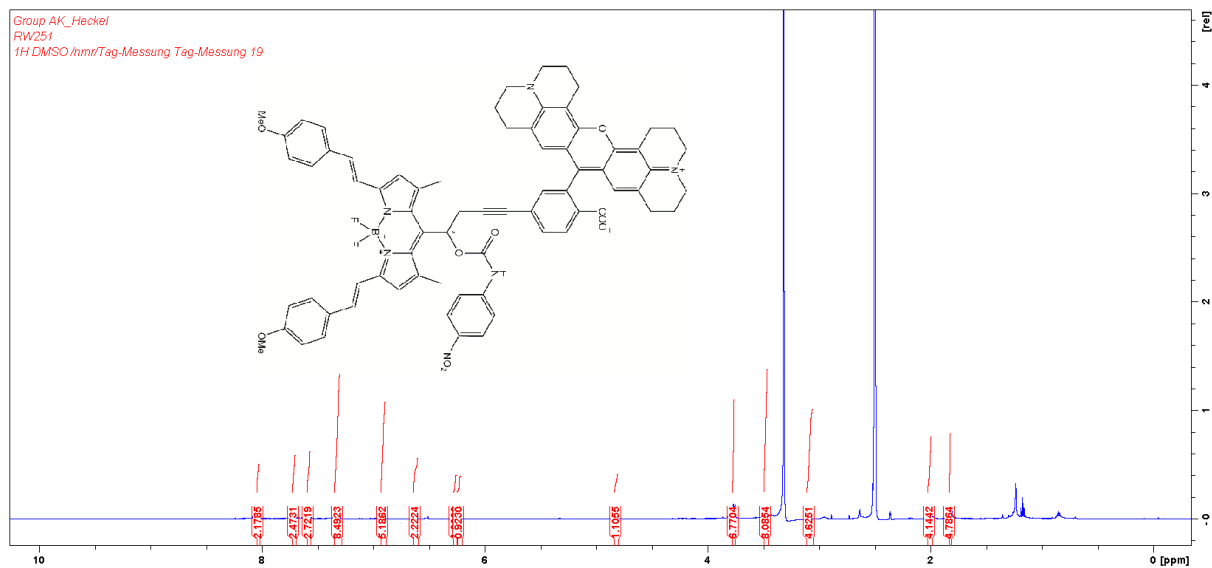
C:\User\...12021\23.03.2021\RW_217_A7

3/23/2021 11:41:04 AM

RW_217_A7 #1-6 RT: 0.01-0.24 AV: 6 NL: 2.92E7
T: FTMS + p MALDI Full ms [500.00-1200.00]



RHO-BPY-PNA

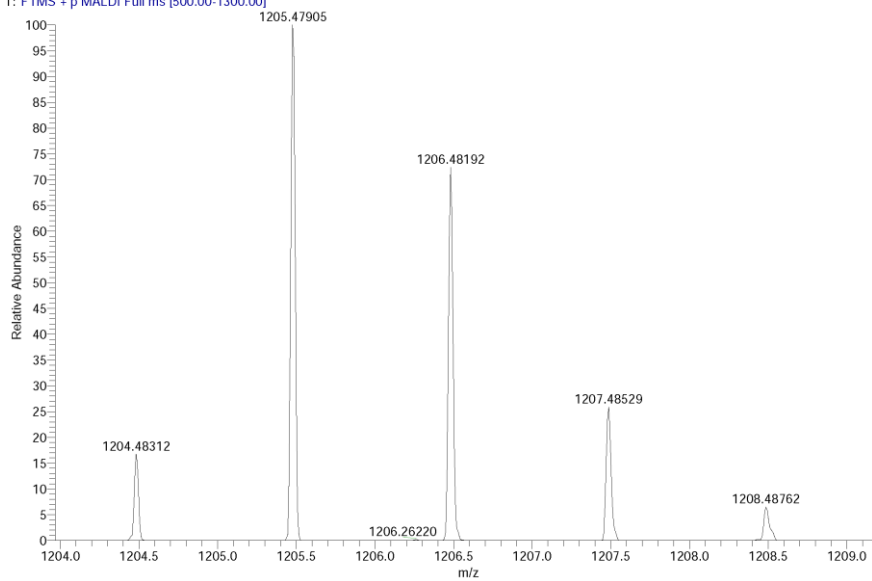


C:\User\...l2021\03.02.2021\RW251_D9

2/3/2021 1:35:54 PM

RW251 mit CICA gemessen.

RW251_D9 #1-7 RT: 0.01-0.29 AV: 7 NL: 6.29E6
T: FTMS + p MALDI Full ms [500.00-1300.00]



References

- (1) Krumova, K.; Cosa, G. Bodipy Dyes with Tunable Redox Potentials and Functional Groups for Further Tethering: Preparation, Electrochemical, and Spectroscopic Characterization. *Journal of the American Chemical Society* **2010**, *132* (49), 17560–17569. <https://doi.org/10.1021/ja1075663>.
- (2) Mudd, G.; Pi, I. P.; Fethers, N.; Dodd, P. G.; Barbeau, O. R.; Auer, M. A General Synthetic Route to Isomerically Pure Functionalized Rhodamine Dyes. *Methods and Applications in Fluorescence* **2015**, *3* (4). <https://doi.org/10.1088/2050-6120/3/4/045002>.
- (3) Xu, C.; Webb, W. W. Measurement of Two-Photon Excitation Cross Sections of Molecular Fluorophores with Data from 690 to 1050 Nm. *Journal of the Optical Society of America B* **1996**, *13* (3), 481. <https://doi.org/10.1364/josab.13.000481>.
- (4) Makarov, N. S.; Drobizhev, M.; Rebane, A. Two-Photon Absorption Standards in the 550–1600 Nm Excitation Wavelength Range. *Optics Express* **2008**, *16* (6), 4029. <https://doi.org/10.1364/oe.16.004029>.
- (5) de Reguardati, S.; Pahapill, J.; Mikhailov, A.; Stepanenko, Y.; Rebane, A. High-Accuracy Reference Standards for Two-Photon Absorption in the 680–1050 Nm Wavelength Range. *Optics Express* **2016**, *24* (8), 9053. <https://doi.org/10.1364/oe.24.009053>.
- (6) Rumi, M.; Perry, J. W. Two-Photon Absorption: An Overview of Measurements and Principles. *Advances in Optics and Photonics* **2010**, *2* (4), 451. <https://doi.org/10.1364/AOP.2.000451>.
- (7) Enderlein, J.; Erdmann, R. Fast Fitting of Multi-Exponential Decay Curves. *Optics Communications* **1997**, *134* (1–6), 371–378. [https://doi.org/10.1016/S0030-4018\(96\)00384-7](https://doi.org/10.1016/S0030-4018(96)00384-7).
- (8) Slavov, C.; Hartmann, H.; Wachtveitl, J. Implementation and Evaluation of Data Analysis Strategies for Time-Resolved Optical Spectroscopy. *Analytical Chemistry* **2015**, *87* (4), 2328–2336. <https://doi.org/10.1021/ac504348h>.
- (9) Frisch, M. J.; Trucks, G. W.; Schlegel, H. B.; Scuseria, G. E.; Robb, M. A.; Cheeseman, J. R.; Scalmani, G.; Barone, V.; Petersson, G. A.; Nakatsuji, H.; Li, X.; Caricato, M.; Marenich, A. v; Bloino, J.; Janesko, B. G.; Gomperts, R.; Mennucci, B.; Hratchian, H. P.; Ortiz, J. v; Izmaylov, A. F.; Sonnenberg, J. L.; Williams-Young, D.; Ding, F.; Lipparini, F.; Egidi, F.; Goings, J.; Peng, B.; Petrone, A.; Henderson, T.; Ranasinghe, D.; Zakrzewski, V. G.; Gao, J.; Rega, N.; Zheng, G.; Liang, W.; Hada, M.; Ehara, M.; Toyota, K.; Fukuda, R.; Hasegawa, J.; Ishida, M.; Nakajima, T.; Honda, Y.; Kitao, O.; Nakai, H.; Vreven, T.; Throssell, K.; Montgomery Jr., J. A.; Peralta, J.

- E.; Ogliaro, F.; Bearpark, M. J.; Heyd, J. J.; Brothers, E. N.; Kudin, K. N.; Staroverov, V. N.; Keith, T. A.; Kobayashi, R.; Normand, J.; Raghavachari, K.; Rendell, A. P.; Burant, J. C.; Iyengar, S. S.; Tomasi, J.; Cossi, M.; Millam, J. M.; Klene, M.; Adamo, C.; Cammi, R.; Ochterski, J. W.; Martin, R. L.; Morokuma, K.; Farkas, O.; Foresman, J. B.; Fox, D. J. Gaussian~16 Revision C.01. 2016.
- (10) Miertuš, S.; Scrocco, E.; Tomasi, J. Electrostatic Interaction of a Solute with a Continuum. A Direct Utilization of AB Initio Molecular Potentials for the Prediction of Solvent Effects. *Chemical Physics* **1981**, *55* (1), 117–129. [https://doi.org/10.1016/0301-0104\(81\)85090-2](https://doi.org/10.1016/0301-0104(81)85090-2).
- (11) Miertuš, S.; Tomasi, J. Approximate Evaluations of the Electrostatic Free Energy and Internal Energy Changes in Solution Processes. *Chemical Physics* **1982**, *65* (2), 239–245. [https://doi.org/10.1016/0301-0104\(82\)85072-6](https://doi.org/10.1016/0301-0104(82)85072-6).
- (12) Aidas, K.; Angeli, C.; Bak, K. L.; Bakken, V.; Bast, R.; Boman, L.; Christiansen, O.; Cimiraglia, R.; Coriani, S.; Dahle, P.; Dalskov, E. K.; Ekström, U.; Enevoldsen, T.; Eriksen, J. J.; Ettenhuber, P.; Fernández, B.; Ferrighi, L.; Fliegl, H.; Frediani, L.; Hald, K.; Halkier, A.; Hättig, C.; Heiberg, H.; Helgaker, T.; Hennum, A. C.; Hettema, H.; Hjertenes, E.; Høst, S.; Høyvik, I.-M.; Iozzi, M. F.; Jansík, B.; Jensen, H. J. Aa.; Jonsson, D.; Jørgensen, P.; Kauczor, J.; Kirpekar, S.; Kjærgaard, T.; Klopper, W.; Knecht, S.; Kobayashi, R.; Koch, H.; Kongsted, J.; Krapp, A.; Kristensen, K.; Ligabue, A.; Lutnæs, O. B.; Melo, J. I.; Mikkelsen, K. v.; Myhre, R. H.; Neiss, C.; Nielsen, C. B.; Norman, P.; Olsen, J.; Olsen, J. M. H.; Osted, A.; Packer, M. J.; Pawłowski, F.; Pedersen, T. B.; Provasi, P. F.; Reine, S.; Rinkevicius, Z.; Ruden, T. A.; Ruud, K.; Rybkin, V. v.; Salek, P.; Samson, C. C. M.; de Merás, A. S.; Saue, T.; Sauer, S. P. A.; Schimmelpfennig, B.; Sneskov, K.; Steindal, A. H.; Sylvester-Hvid, K. O.; Taylor, P. R.; Teale, A. M.; Tellgren, E. I.; Tew, D. P.; Thorvaldsen, A. J.; Thøgersen, L.; Vahtras, O.; Watson, M. A.; Wilson, D. J. D.; Ziolkowski, M.; Ågren, H. The Dalton Quantum Chemistry Program System. *WIREs Computational Molecular Science* **2014**, *4* (3), 269–284. <https://doi.org/10.1002/wcms.1172>.
- (13) Tamura, H.; Mallet, J.-M.; Oheim, M.; Burghardt, I. Ab Initio Study of Excitation Energy Transfer between Quantum Dots and Dye Molecules. *The Journal of Physical Chemistry C* **2009**, *113* (18), 7548–7552. <https://doi.org/10.1021/jp811042t>.
- (14) McWeeny, R. *Methods of Molecular Quantum Mechanics*, 2. Aufl.; Academic Press: London, 1992.
- (15) Krueger, B. P.; Scholes, G. D.; Fleming, G. R. Calculation of Couplings and Energy-Transfer Pathways between the Pigments of LH2 by the Ab Initio Transition Density Cube Method.

The Journal of Physical Chemistry B **1998**, *102* (27), 5378–5386.

<https://doi.org/10.1021/jp9811171>.

- (16) Shao, Y.; Gan, Z.; Epifanovsky, E.; Gilbert, A. T. B.; Wormit, M.; Kussmann, J.; Lange, A. W.; Behn, A.; Deng, J.; Feng, X.; Ghosh, D.; Goldey, M.; Horn, P. R.; Jacobson, L. D.; Kaliman, I.; Khaliullin, R. Z.; Kuś, T.; Landau, A.; Liu, J.; Proynov, E. I.; Rhee, Y. M.; Richard, R. M.; Rohrdanz, M. A.; Steele, R. P.; Sundstrom, E. J.; Woodcock, H. L.; Zimmerman, P. M.; Zuev, D.; Albrecht, B.; Alguire, E.; Austin, B.; Beran, G. J. O.; Bernard, Y. A.; Berquist, E.; Brandhorst, K.; Bravaya, K. B.; Brown, S. T.; Casanova, D.; Chang, C.-M.; Chen, Y.; Chien, S. H.; Closser, K. D.; Crittenden, D. L.; Diedenhofen, M.; DiStasio, R. A.; Do, H.; Dutoi, A. D.; Edgar, R. G.; Fatehi, S.; Fusti-Molnar, L.; Ghysels, A.; Golubeva-Zadorozhnaya, A.; Gomes, J.; Hanson-Heine, M. W. D.; Harbach, P. H. P.; Hauser, A. W.; Hohenstein, E. G.; Holden, Z. C.; Jagau, T.-C.; Ji, H.; Kaduk, B.; Khistyayev, K.; Kim, J.; Kim, J.; King, R. A.; Klunzinger, P.; Kosenkov, D.; Kowalczyk, T.; Krauter, C. M.; Lao, K. U.; Laurent, A. D.; Lawler, K. v.; Levchenko, S. v.; Lin, C. Y.; Liu, F.; Livshits, E.; Lochan, R. C.; Luenser, A.; Manohar, P.; Manzer, S. F.; Mao, S.-P.; Mardirossian, N.; Marenich, A. v.; Maurer, S. A.; Mayhall, N. J.; Neuscammann, E.; Oana, C. M.; Olivares-Amaya, R.; O'Neill, D. P.; Parkhill, J. A.; Perrine, T. M.; Peverati, R.; Prociuk, A.; Rehn, D. R.; Rosta, E.; Russ, N. J.; Sharada, S. M.; Sharma, S.; Small, D. W.; Sodt, A.; Stein, T.; Stück, D.; Su, Y.-C.; Thom, A. J. W.; Tsuchimochi, T.; Vanovschi, V.; Vogt, L.; Vydrov, O.; Wang, T.; Watson, M. A.; Wenzel, J.; White, A.; Williams, C. F.; Yang, J.; Yeganeh, S.; Yost, S. R.; You, Z.-Q.; Zhang, I. Y.; Zhang, X.; Zhao, Y.; Brooks, B. R.; Chan, G. K. L.; Chipman, D. M.; Cramer, C. J.; Goddard, W. A.; Gordon, M. S.; Hehre, W. J.; Klamt, A.; Schaefer, H. F.; Schmidt, M. W.; Sherrill, C. D.; Truhlar, D. G.; Warshel, A.; Xu, X.; Aspuru-Guzik, A.; Baer, R.; Bell, A. T.; Besley, N. A.; Chai, J.-D.; Dreuw, A.; Dunietz, B. D.; Furlani, T. R.; Gwaltney, S. R.; Hsu, C.-P.; Jung, Y.; Kong, J.; Lambrecht, D. S.; Liang, W.; Ochsenfeld, C.; Rassolov, V. A.; Slipchenko, L. v.; Subotnik, J. E.; van Voorhis, T.; Herbert, J. M.; Krylov, A. I.; Gill, P. M. W.; Head-Gordon, M. Advances in Molecular Quantum Chemistry Contained in the Q-Chem 4 Program Package. *Molecular Physics* **2015**, *113* (2), 184–215. <https://doi.org/10.1080/00268976.2014.952696>.
- (17) Tamura, H.; Martinazzo, R.; Ruckebauer, M.; Burghardt, I. Quantum Dynamics of Ultrafast Charge Transfer at an Oligothiophene-Fullerene Heterojunction. *The Journal of Chemical Physics* **2012**, *137* (22), 22A540. <https://doi.org/10.1063/1.4751486>.